International Journal of Engineering Science 217 (2025) 104384

Contents lists available at ScienceDirect

International Journal of Engineering Science

journal homepage: www.elsevier.com/locate/ijengsci

Full length article

Predictive asymptotic models of damage evolution in thin adhesives with tension–compression asymmetry

Michele Serpilli [a], Raffaella Rizzoni [b,*], Frédéric Lebon [c]

[a] Department of Civil and Building Engineering, and Architecture, Università Politecnica delle Marche, Ancona, Italy
[b] Department of Engineering, University of Ferrara, Ferrara, Italy
[c] LMA, Aix Marseille University, CNRS, Centrale Marseille, Marseille, France

ARTICLE INFO

Keywords:
Interface damage model
Asymptotic analysis
tension–compression asymmetry
Micromechanics
Adhesive joints
Continuum damage mechanics

ABSTRACT

In structural engineering, accurate modeling of material damage is crucial, particularly the tension–compression asymmetry observed in quasi-brittle materials and adhesive joints. While cohesive interface models are commonly employed in the analysis of bonded structures, the parameters of these models frequently lack a direct correlation with the physical properties of the adhesive layer. To address this issue and capture the tension–compression asymmetry, this study uses asymptotic analysis to derive two new interface damage models (termed F1d and F2d) from a thin damaging interphase. The proposed models are formulated within a thermodynamically consistent framework. The F1d model uses a single damage variable with an asymmetric evolution law, whereas the more advanced F2d model uses separate variables for tensile and compressive damage, enabling independent evolution kinetics. To bridge the gap between scales and link macroscopic damage to micro-defect evolution, the new models are coupled with two micromechanical schemes: the non-interacting Kachanov–Sevostianov model and the Mori–Tanaka–Benveniste model, the latter of which accounts for defect interactions. The theoretical formulations of the models are presented, and their predictive capabilities are demonstrated through numerical simulations of a bonded joint under axial loading.

1. Introduction

Predictive modeling of material damage and failure is crucial in structural engineering. Among the various approaches, Continuum Damage Mechanics (CDM) is a powerful framework for describing the progressive loss of stiffness and strength in materials under load caused by the nucleation and growth of micro-defects, such as voids and cracks (Lemaitre, 1985; Lemaitre, Chaboche, Benallal, & Desmorat, 2009; Park, Ahmed, & Voyiadjis, 2021). A key challenge in CDM is formulating models that capture overall softening behavior and accurately represent material-specific characteristics, such as distinct responses to tensile versus compressive stress. This tension–compression asymmetry, also known as "(quasi) unilateral effect" or "microdefects/crack closure effect" (Fassin, Eggersmann, Wulfinghoff, & Reese, 2019; Murakami, 1988), is a prominent feature of many engineering materials. It is most notable in quasi-brittle materials such as concrete (Frémond & Nedjar, 1995; Mazars, Berthaud, & Ramtani, 1990), but also occurs in ductile materials such as metals (Wei, Gerke, & Brünig, 2023; Wei, Zistl, Gerke, & Brünig, 2022), composite adhesive joints (Yang, Yan, Liu, & Ran, 2012; Zhang, Ramesh, & Chin, 2008) and polymers (Liu et al., 2021), where different failure mechanisms are observed under different loading conditions. More specifically, in concrete, damage under tension is typically dominated by the opening and coalescence of microcracks, resulting in a rapid, brittle-like damage. In contrast, under compression,

* Correspondence to: Department of Engineering, University of Ferrara, Via Saragat 1, 44122 Ferrara, Italy.
E-mail address: raffaella.rizzoni@unife.it (R. Rizzoni).

https://doi.org/10.1016/j.ijengsci.2025.104384
Received 21 July 2025; Received in revised form 3 September 2025; Accepted 4 September 2025
Available online 18 September 2025

damage involves a more complex process of microcrack closure, frictional sliding, and pore collapse (Mazars & Pijaudier-Cabot, 1989; Shah, Swartz, & Ouyang, 1995; Van Mier, 1996). This results in significantly higher compressive strength and a more progressive, pseudo-ductile failure mode.

Accurately capturing this asymmetry is essential in numerical simulations and for a realistic analysis of structures subjected to complex loading, as it prevents the prediction of compressive dominant failure and ensures a more realistic representation of damage and fracture behavior. A widely adopted strategy involves incorporating tension–compression asymmetry through energy decompositions, thereby enabling a directional distinction in damage driving forces. Some examples are: the spectral decomposition (Miehe, Welschinger, & Hofacker, 2010), which decomposes the elastic strain energy density by distinguishing between positive and negative eigenvalues of the strain tensor; the volumetric-deviatoric decomposition (Amor, Marigo, & Maurini, 2009; Lancioni & Royer-Carfagni, 2009), where the degradable energy is expressed by the deviatoric part of the strain tensor; the star-convex model (Vicentini, Zolesi, Carrara, Maurini, & De Lorenzis, 2024), in which the residual energy density only depends on the negative trace of the strain tensor. For more details on refined tension–compression asymmetry phase-field theories, the reader can refer to Zhang, Han, Zhang, Reese, and Brepols (2025). As it will be specified in the sequel, the present work will adopt the spectral decomposition strategy to take into account this asymmetry.

To address problems in bonded structures, several approaches are available in the literature (Kumar & Mittal, 2013; Ries, 2024; Tserpes et al., 2022). Among these, interface models are widely used in many engineering disciplines. These models can simulate various phenomena, including cohesive fracture, delamination in composites, strain localization and the bond between structural components (Abrate, Ferrero, & Navarro, 2015; Alfano & Crisfield, 2001; Barenblatt, 1962; Corigliano, 1993; Elices, Guinea, Gomez, & Planas, 0000; Needleman, 1990; Park & Paulino, 2011). A key feature of Cohesive Zone Models (CZMs) is the characterization of a physically thin layer, such as an adhesive bond, as a zero-thickness surface. The constitutive behavior is then described by a relationship linking the continuous traction across the interface to the displacement field jump. Although simple linear relationships can be employed, interface laws can also incorporate complex nonlinear effects, including damage, plasticity and viscous phenomena. This results in a wide range of models being presented in the scientific literature, see for example Alfano and Sacco (2006), Cazes, Simatos, Coret, and Combescure (2010), Corigliano and Ricci (2001), Kim (2011) and Xu and Lu (2013) and the references therein.

A major limitation of CZMs is that the material parameters of the cohesive interface law are often unrelated to the physics of the thin layer being modeled. One way to overcome this problem is the use of the asymptotic methods (Ciarlet, 1997; Sánchez-Palencia, 1980). These techniques can be employed to obtain interface models starting from a thin interphase with vanishing thickness and a variety of constitutive behaviors that can be linked to the microstructure of the material. The resulting imperfect interface model is expressed in terms of transmission conditions associated with jumps in the traction and displacement fields, inheriting the material properties of the thin interphase. The development of interface models via asymptotic techniques has been advanced by various mathematical approaches. These include classical variational methods (Benveniste, 1987; Benveniste & Miloh, 1986; Javili, Kaessmair, & Steinmann, 2014) and techniques such as asymptotic expansion methods, which have been applied in linear (Geymonat, Hendili, Krasucki, Serpilli, & Vidrascu, 2014; Lebon & Rizzoni, 2010, 2011; Rizzoni, Dumont, Lebon, & Sacco, 2014; Serpilli & Lenci, 2016) and nonlinear elasticity (Krasucki, Münch, & Ousset, 2004; Rizzoni, Dumont, & Lebon, 2017). The scope has since expanded to the contact of rough surfaces (Raffa, Lebon, & Vairo, 2016) damaging materials (Bonetti, Bonfanti, Lebon, & Rizzoni, 2017; Raffa, Lebon, & Rizzoni, 2022), and multiphysics theories (Bauzet, Dumont, Lebon, & Nabet, 2025; Dumont, Serpilli, Rizzoni, & Lebon, 2020; Rizzoni, Serpilli, Raffa, & Lebon, 2023; Serpilli, 2014; Serpilli, Rizzoni, Lebon, & Dumont, 2019).

Motivated by these considerations, this work introduces two novel interface damage models, denoted with F1d and F2d, designed to describe the behavior of thin adhesive layers joining two linear elastic adherents, by means of the asymptotic expansions method. The underlying constitutive models have been formulated within a thermodynamically consistent framework and are able to represent tension–compression asymmetry (Freddi & Frémond, 2006; Frémond, 2002; Frémond & Nedjar, 1995, 1996), through the aforementioned spectral decomposition of the strain tensor into positive and negative parts. The proposed damage evolution models generalize those introduced in Frémond's theory (Frémond, 2002) and are applied to thin interphase layers. More specifically, the F1d model employs a single damage variable, ρ, but incorporates asymmetry through the structure of the damage evolution law. The F2d model is characterized by a more advanced damage description, that introduces separate internal variables for tensile, ρ_t, and compressive, ρ_c, damage. This allows for independent control over their respective initiation thresholds and evolution kinetics. The main objective of this paper is to present the complete theoretical formulation of the model F1d and F2d models and to prove their qualitative and predictive capabilities through numerical examples on a benchmark problem. A rigorous calibration against specific experimental data is intended as the subject of future work.

To relate macroscopic damage to material degradation at the microscale, the two frameworks are coupled with two distinct micromechanical schemes: the non-interacting Kachanov-Sevostianov (KS) approximation (Kachanov, 1994; Kachanov & Sevostianov, 2018; Kachanov, Tsukrov, & Shafiro, 1994; Pronina, Narykova, & Kachanov, 2025), and the Mori–Tanaka-Benveniste (MTB) model (Mori & Tanaka, 1973; Pronina et al., 2025), the latter of accounts for defect interactions. This paper presents the theoretical formulation of these models and demonstrates their predictive capabilities by means of numerical simulations of a joint undergoing tensile and compressive loadings. Notably, the KS and MTB schemes provide the crucial link between the damage variable(s), ρ (or ρ_t, ρ_c), and the effective elastic moduli of the adhesive. The derivatives of these moduli enter the damage evolution law, that is the asymptotic limit of the damage evolution law in the three-dimensional Frémond's models.

The coupling of the continuum damage framework with the KS and MTB micromechanical schemes relies on a two-step approach. We have three distinct scales (or even four, if we consider microcracks): the structure (macroscale, characteristic dimension, say L), the interphase (mesoscale, characteristic dimension, say h^ε) and the material (microstructure, characteristic dimension, say η), with $\eta \ll h^\varepsilon \ll L$. In our two-step methodology, we first perform 'homogenization' at the microstructure scale (transition to the

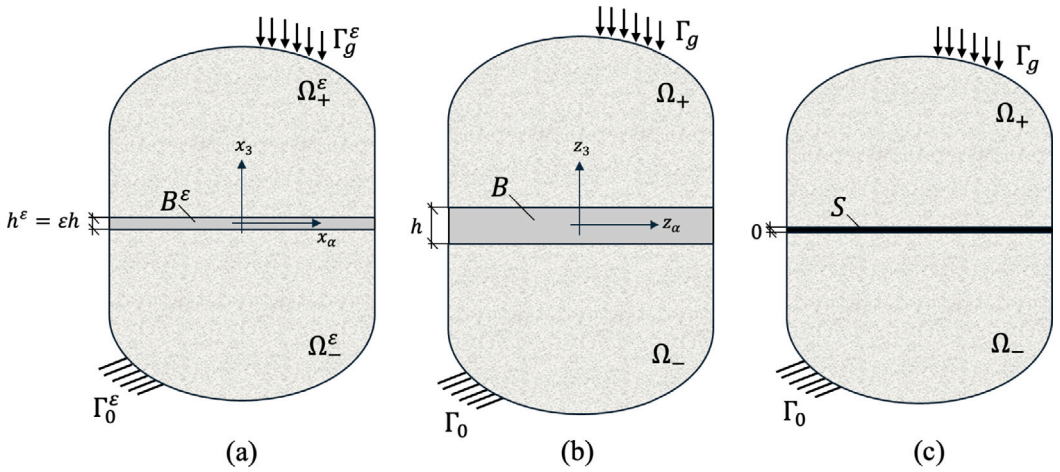

Fig. 1. Geometry of the bonded assembly composed of two adherent bodies and an adhesive thin layer: reference configuration (a), rescaled configuration (b) and limit configuration (c).

mesoscale, via the KS or MTB schemes) and then 'homogenization' in the direction of the adhesive thickness (transition to the macroscale). This two-step approach is standard in multi-scale mechanics for deriving simplified structural models from complex microstructured continua, see for example Ponte Castañeda and Willis (1995).

Our methodology is related to, yet distinct from, micromechanical approaches, where the damage criterion is formulated directly as an energy release rate derived from the homogenized potential energy of the cracked material. Dormieux et al. proposed an example of this approach (Dormieux, Kondo, & Ulm, 2006). Pichler et al. proposed an alternative methodology that links micromechanics and damage evolution (Pichler, Hellmich, & A. Mang, 2007). In their study, they combined propagation criteria for a single penny-shaped crack embedded in an infinite matrix and subjected to remote stresses with the dilute and Mori–Tanaka micromechanical schemes. These combinations implicitly define a rate-independent damage evolution law, enabling the full strain-softening curve to be derived. While all these methods aim to incorporate microstructural information into a continuum model, they differ fundamentally in their starting points: a microscopic stress criterion (Pichler et al., 2007); a macroscopic energy criterion (Dormieux et al., 2006); or a thermodynamically derived kinetic law, as in Freddi and Frémond (2006), Frémond (2002) and Frémond and Nedjar (1995, 1996) and in the present work. This results in different types of damage evolution: rate-independent (Dormieux et al., 2006; Pichler et al., 2007) versus rate-dependent (Freddi & Frémond, 2006; Frémond, 2002; Frémond & Nedjar, 1995, 1996).

The paper is organized as follows. Section 2 presents the overview of the equilibrium problem of an assembly made of two bodies, adhesively joint with a damaging thin layer. The F1d and F2d damage evolution equations are respectively presented. Section 3 deals with the asymptotic expansions method and the derivation of the two damage evolution limit models. To numerically assess the damage models, a benchmark problem of a composite medium subjected to tensile and compressive axial loads is presented in Section 4, highlighting the main differences between F1d and F2d, and using two different micromechanical homogenization schemes (KS and MTB, respectively). Finally, Section 5 is devoted to the concluding remarks.

2. Overview of the problem

In the sequel, Greek indices range in the set $\{1,2\}$, Latin indices range in the set $\{1,2,3\}$, and Einstein's summation convention with respect to repeated indices is adopted. The following notations for the scalar and dyadic products are also introduced: $\mathbf{a}\cdot\mathbf{b} := a_ib_i$, $(\mathbf{a}\otimes\mathbf{b})_{ij} := a_ib_j$, and $(\mathbf{a}\odot\mathbf{b})_{ij} := \frac{1}{2}(a_ib_j + a_jb_i)$, for all vectors $\mathbf{a} = (a_i)$ and $\mathbf{b} = (b_i)$. Moreover, we note with $\langle f\rangle_\pm := \mathrm{Max}\{0, \pm f\}$ the positive and negative part of the scalar function f, respectively, equivalent to the Macaulay's brackets, and $\mathbf{A}^\pm = (A^\pm_{ij})$ the positive and negative parts of tensor $\mathbf{A}$, obtained after diagonalization (for more details, see Appendix).

Let us consider a composite structure made of three media, two adherents and a thin adhesive layer, occupying a smooth bounded domain $\Omega^\varepsilon \subset \mathbb{R}^3$, as depicted in Fig. 1(a).

The domain Ω^ε depends on the parameter ε in a sense which will be made precise later. An orthonormal Cartesian frame $(O, \mathbf{e}_1, \mathbf{e}_2, \mathbf{e}_3)$ is introduced and the triplet (x_1, x_2, x_3) is taken to denote the three coordinates of a material point. The adhesive occupies the domain B^ε, defined as $B^\varepsilon := \left\{(x_1,x_2,x_3)\in\Omega^\varepsilon : |x_3| < \frac{h^\varepsilon}{2}\right\}$, with thickness h^ε, whose plane mid-surface is $S = \{(x_1,x_2,x_3)\in\Omega^\varepsilon : x_3 = 0\}$, modeling the interface in the limit problem. The adherents occupy the domains $\Omega^\varepsilon_\pm = \left\{(x_1,x_2,x_3)\in\Omega^\varepsilon : \pm x_3 > \frac{h^\varepsilon}{2}\right\}$. The interfaces between the adhesive and the adherents are denoted with $S^\varepsilon_\pm = \left\{(x_1,x_2,x_3)\in\Omega^\varepsilon : x_3 = \pm\frac{h^\varepsilon}{2}\right\}$. The assembly is subjected to body forces $\mathbf{f}^\varepsilon$, acting in $\Omega^\varepsilon_\pm$, and surface forces $\mathbf{g}^\varepsilon$, applied to the partition of the boundary $\Gamma^\varepsilon_g \subset \partial\Omega^\varepsilon$ with strictly positive measure. The composite is fully clamped on a portion of the boundary $\Gamma^\varepsilon_0 \subset \partial\Omega^\varepsilon$. The boundary sets

Γ_g^ϵ and Γ_0^ϵ are assumed to be located far from the interphase. Body forces are neglected in B^ϵ. Suitable regularity assumptions are made on the external loads to ensure the wellposedness of the equilibrium problem.

In the sequel, $\mathbf{u}^\epsilon = (u_i^\epsilon)$ denotes the displacement field, while $\mathbf{e}^\epsilon$ denotes the linearized strain tensor, with components $e_{ij}^\epsilon := \frac{1}{2}(u_{i,j}^\epsilon + u_{j,i}^\epsilon)$. Notation $(\cdot)_{,i}$ represents the partial derivative with respect to x_i. The two adherents and the adhesive are made of linearly elastic materials, whose constitutive laws are defined as follows:

$$\sigma_{ij}^\epsilon = C_{ijkl}^\epsilon e_{kl}^\epsilon, \tag{1}$$

where $\boldsymbol{\sigma}^\epsilon = (\sigma_{ij}^\epsilon)$ and C_{ijkl}^ϵ represents the Cauchy's stress tensor and the elastic constants, respectively. The elasticity tensor satisfies the classical major and minor symmetries properties. We suppose that the material of the adhesive is damaging, with distinct and different damage behaviors under tension and compression.

As customary, the governing equations of the equilibrium problem, paired with the constitutive laws (1), can be written :

$$\begin{cases} \sigma_{ij,j}^\epsilon + f_i^\epsilon = 0 & \text{in } \Omega^\epsilon, \\ \sigma_{ij}^\epsilon n_j^\epsilon = g_i^\epsilon & \text{on } \Gamma_g^\epsilon, \\ [[\sigma_{i3}^\epsilon]] = 0 & \text{on } S_\pm^\epsilon, \\ [[u_i^\epsilon]] = 0 & \text{on } S_\pm^\epsilon, \\ u_i^\epsilon = 0 & \text{on } \Gamma_0^\epsilon. \end{cases} \tag{2}$$

In the sequel, the notation $\bar{f}$, $\hat{f}$ stands for the restriction of function f in the adherents and in the adhesive, respectively. In (2), $[[f]]$ denotes the jump function at the interfaces $S_\pm^\epsilon$, i.e $[[f]] := \bar{f}(\pm h^\epsilon/2) - \hat{f}(\pm h^\epsilon/2)$.

The above equations needs to be coupled with the evolution damage equation inside the adhesive layer. It is assumed that the constitutive parameters depend on one or two damage parameters, usually indicate with ρ, which can be thought as a micro-crack or micro-voids volumetric density. In particular, two different damage evolution models will be considered in the asymptotic analysis, based on Frémond's damage theory (Frémond, 2002): (i) the Frémond's 1-damage parameter (F1d) evolution model (Frémond & Nedjar, 1995, 1996); (ii) the Frémond's 2-damage parameters (F2d) evolution model (Frémond & Nedjar, 1995, 1996). The above damage models allows to distinguish the damage evolution behavior under tensile and compressive loads.

The following subsections details the thermodynamically consistent derivation of the state and damage evolution laws from a postulated free energy potential and a pseudo-potential of dissipation, following the approach proposed by Frémond.

The F1d evolution model

The adhesive material is assumed to be linear elastic, depending on one damage parameter $\rho \in [0,1]$. The asymmetry between tension and compression is induced by the damage variable. In particular, we consider the following free energy Ψ_1^ϵ:

$$\Psi_1^\epsilon = \frac{1}{2}\left(2\hat{\mu}^\epsilon(\rho)\hat{e}_{ij}^\epsilon \hat{e}_{ij}^\epsilon + \hat{\lambda}^\epsilon(\rho)(\hat{e}_s^\epsilon)^2\right) - \hat{\omega}^\epsilon(\rho) + I_{[0,1]}(\rho), \tag{3}$$

where $\hat{\lambda}^\epsilon$ and $\hat{\mu}^\epsilon$ the Lamé's constants, depending on ρ, $\hat{e}_s^\epsilon := \mathrm{Tr}\,\hat{\mathbf{e}}^\epsilon = \hat{e}_{11}^\epsilon + \hat{e}_{22}^\epsilon + \hat{e}_{33}^\epsilon$ is the trace of the strain tensor, $\omega^\epsilon = \omega^\epsilon(\rho) < 0$ denotes the damage initiation threshold expressed as a volumetric energy, similar to Dupré's energy, cf. Frémond (2002), and I_A is the indicator function of the set A, i.e. $I_A(x) = 0$ if $x \in A$ and $I_A(x) = +\infty$ otherwise. The constitutive equation for the damaging adhesive can be obtain as follows:

$$\hat{\sigma}_{ij}^\epsilon = \frac{\partial \Psi_1^\epsilon}{\partial \hat{e}_{ij}^\epsilon} = 2\hat{\mu}^\epsilon(\rho)\hat{e}_{ij}^\epsilon + \hat{\lambda}^\epsilon(\rho)\hat{e}_{pp}^\epsilon \delta_{ij}, \tag{4}$$

with δ_{ij} the Kronecker's symbol. The evolution of the damage parameter is introduced through a pseudo-potential of dissipation, considering a generalization of the Frémond's theory with one damage parameter (Frémond & Nedjar, 1995):

$$\Phi_1^\epsilon = \frac{1}{2}\hat{\eta}^\epsilon \dot{\rho}^2 - \frac{1}{2}\dot{\rho}\left(2\hat{\mu}_{,\rho}^\epsilon(\rho)\hat{e}_{ij}^{-,\epsilon}\hat{e}_{ij}^{-,\epsilon} + \hat{\lambda}_{,\rho}^\epsilon(\rho)\langle\hat{e}_s^\epsilon\rangle_-^2\right) + I_{[0,+\infty)}(\dot{\rho}), \tag{5}$$

where $\hat{\eta}^\epsilon$ is a positive viscosity parameter. The effect of the indicator function is to make it compulsory for $\dot{\rho}$ to be non-negative and, thus, the degradation of the adhesive is an irreversible process. The form of the pseudo-potential of dissipation is chosen such that damage results only from extensions.

By means of the Clausius-Duhem relation

$$\frac{\partial \Psi_1^\epsilon}{\partial \rho} + \frac{\partial \Phi_1^\epsilon}{\partial \dot{\rho}} \ni 0, \tag{6}$$

the F1d model damage evolution equations can be written in the following form:

$$\hat{\eta}^\epsilon \dot{\rho} = \left\langle \hat{\omega}_{,\rho}^\epsilon(\rho) - \frac{1}{2}\left(2\hat{\mu}_{,\rho}^\epsilon(\rho)\hat{e}_{ij}^{+,\epsilon}\hat{e}_{ij}^{+,\epsilon} + \hat{\lambda}_{,\rho}^\epsilon(\rho)\langle\hat{e}_s^\epsilon\rangle_+^2\right)\right\rangle_+ . \tag{7}$$

Remark 1. The proposed model represents a generalization of the damage theory, proposed by Frémond and Nedjar (1995). Indeed, by considering the simple case of a linear dependence of the elastic coefficients with respect to damage parameter ρ, i.e. $\hat{\lambda}^\epsilon(\rho) = (1-\rho)\hat{\lambda}^\epsilon$ and $\hat{\mu}^\epsilon(\rho) = (1-\rho)\hat{\mu}^\epsilon$, and the explicit expression for the threshold energy, $\hat{\omega}^\epsilon(\rho) = \hat{w}^\epsilon\rho + M^\epsilon(\log(1-\rho)+\rho)$, it is

possible to recover the initial model proposed in Frémond and Nedjar (1995). With these assumptions, $\hat{\lambda}^{\epsilon}_{,\rho}(\rho) = -\hat{\lambda}^{\epsilon}$ and $\hat{\mu}^{\epsilon}_{,\rho}(\rho) = -\hat{\mu}^{\epsilon}$, $\hat{\omega}^{\epsilon}_{,\rho}(\rho) = \hat{w}^{\epsilon} - M^{\epsilon}\frac{\rho}{1-\rho}$ and thus,

$$\hat{\eta}^{\epsilon}\dot{\rho} = \left\langle \hat{w}^{\epsilon} - M^{\epsilon}\frac{\rho}{1-\rho} + \frac{1}{2}\left(2\hat{\mu}^{\epsilon}\hat{e}^{+,\epsilon}_{ij}\hat{e}^{+,\epsilon}_{ij} + \hat{\lambda}^{\epsilon}\langle\hat{e}^{\epsilon}_{s}\rangle^{2}_{+}\right)\right\rangle_{+}. \tag{8}$$

The above expression is formally equivalent to cf. Frémond and Nedjar (1995, Eq. (12)), with the choice $\rho = 1-\beta$ for the damage parameter.

The F2d evolution model

When damage is produced, microcracks appear in the zones where extensions exist. When changing the sign of the principal deformations by changing the sign of the loading, these microcracks close. In the previous damage model, the unilateral behavior appears only at the macroscopic (global) level, while the closure of microcracks in compression gives rise to a unilateral phenomenon at the microscale, as highlighted by the experiments. Hence, following Frémond's approach, two distinct damage parameter $\rho_t,\ \rho_c \in [0,1]$ in tension and compression are respectively considered. The adhesive material is assumed to be linear elastic isotropic. In particular, let us consider the following free energy Ψ^{ϵ}_2:

$$\begin{aligned}\Psi^{\epsilon}_2 = {}& \tfrac{1}{2}\left(2\hat{\mu}^{\epsilon}(\rho_t)\hat{e}^{+,\epsilon}_{ij}\hat{e}^{+,\epsilon}_{ij} + \hat{\lambda}^{\epsilon}(\rho_t)\langle\hat{e}^{\epsilon}_{s}\rangle^{2}_{+} + 2\hat{\mu}^{\epsilon}(\rho_c)\hat{e}^{-,\epsilon}_{ij}\hat{e}^{-,\epsilon}_{ij} + \hat{\lambda}^{\epsilon}(\rho_c)\langle\hat{e}^{\epsilon}_{s}\rangle^{2}_{-}\right)\\ & -\hat{\omega}^{\epsilon}_{t}(\rho_t) - \hat{\omega}^{\epsilon}_{c}(\rho_c) + I_C(\rho_t,\rho_c),\end{aligned} \tag{9}$$

where $(\rho_t,\rho_c) \in C := \{(x,y),\ x\in[0,1],\ y\in[0,1],\ x\le y\}$, $\hat{\omega}^{\epsilon}_{t} = \hat{\omega}^{\epsilon}_{t}(\rho_t)$ and $\hat{\omega}^{\epsilon}_{c} = \hat{\omega}^{\epsilon}_{c}(\rho_c)$ are the negative damage initiation thresholds in tension and compression, respectively. The pseudo-potential of dissipation, considering the Frémond's theory with two damage parameters (Frémond & Nedjar, 1995) takes the following form:

$$\Phi^{\epsilon}_2 = \frac{1}{2}\left(\hat{\eta}^{\epsilon}_{t}\dot{\rho_t}^{2} + \hat{\eta}^{\epsilon}_{c}\dot{\rho_c}^{2}\right) - \frac{1}{2}\dot{\rho_c}\left(\hat{\lambda}^{\epsilon}_{,\rho_c}(\rho_c)\langle\hat{e}^{\epsilon}_{s}\rangle^{2}_{-}\right) + I_{[0,+\infty)^2}(\dot{\rho_t},\dot{\rho_c}), \tag{10}$$

where $\hat{\eta}^{\epsilon}_{t}$ and $\hat{\eta}^{\epsilon}_{c}$ are the viscosity parameters in tension and compression, respectively. The constitutive equation for the damaging adhesive can be obtain as follows:

$$\hat{\sigma}^{\epsilon}_{ij} = \frac{\partial\Psi^{\epsilon}_2}{\partial e^{\epsilon}_{ij}} = 2\hat{\mu}^{\epsilon}(\rho_t)\hat{e}^{+,\epsilon}_{ij} + \hat{\lambda}^{\epsilon}(\rho_t)\langle\hat{e}^{\epsilon}_{s}\rangle_{+}\delta_{ij} - (2\hat{\mu}^{\epsilon}(\rho_c)\hat{e}^{-,\epsilon}_{ij} + \hat{\lambda}^{\epsilon}(\rho_t)\langle\hat{e}^{\epsilon}_{s}\rangle_{-}\delta_{ij}). \tag{11}$$

Taking into account the Clausius-Duhem relations:

$$\frac{\partial\Psi^{\epsilon}_2}{\partial\rho_t} + \frac{\partial\Phi^{\epsilon}_2}{\partial\dot{\rho}_t} \ni 0, \quad \frac{\partial\Psi^{\epsilon}_2}{\partial\rho_c} + \frac{\partial\Phi^{\epsilon}_2}{\partial\dot{\rho}_c} \ni 0, \tag{12}$$

we get:

$$\begin{aligned}\hat{\eta}^{\epsilon}_{t}\dot{\rho}_t &= \left\langle \hat{\omega}^{\epsilon}_{t,\rho_t}(\rho_t) - \frac{1}{2}\left(2\hat{\mu}^{\epsilon}_{,\rho_t}(\rho_t)\hat{e}^{+,\epsilon}_{ij}\hat{e}^{+,\epsilon}_{ij} + \hat{\lambda}^{\epsilon}_{,\rho_t}(\rho_t)\langle\hat{e}^{\epsilon}_{s}\rangle^{2}_{+}\right)\right\rangle_{+},\\ \hat{\eta}^{\epsilon}_{c}\dot{\rho}_c &= \left\langle \hat{\omega}^{\epsilon}_{c,\rho_c}(\rho_c) - \frac{1}{2}\left(2\hat{\mu}^{\epsilon}_{,\rho_c}(\rho_c)\hat{e}^{-,\epsilon}_{ij}\hat{e}^{-,\epsilon}_{ij}\right)\right\rangle_{+}.\end{aligned} \tag{13}$$

Remark 2. The present model generalizes the two-damage parameter theory, proposed by Frémond and Nedjar (1996). Indeed, by considering the hypothesis of $\hat{\lambda}^{\epsilon}(\rho_t) = (1-\rho_t)\hat{\lambda}^{\epsilon}$ and $\hat{\mu}^{\epsilon}(\rho_t) = (1-\rho_t)\hat{\mu}^{\epsilon}$ (same for $\hat{\lambda}^{\epsilon}(\rho_c)$ and $\hat{\mu}^{\epsilon}(\rho_c)$), and the explicit expression for the threshold energy, $\hat{\omega_t}^{\epsilon}(\rho_t) = \hat{w}^{\epsilon}_{t}\rho_t + M^{\epsilon}_{t}(\log(1-\rho_t)+\rho_t)$ (same for $\hat{\omega_c}^{\epsilon}(\rho_c)$), it is possible to recover the initial model proposed. Thus,

$$\begin{aligned}\hat{\eta}^{\epsilon}_{t}\dot{\rho}_t &= \left\langle \hat{w}^{\epsilon}_{t} - M^{\epsilon}_{t}\frac{\rho_t}{1-\rho_t} - \frac{1}{2}\left(2\hat{\mu}^{\epsilon}_{,\rho_t}(\rho_t)\hat{e}^{+,\epsilon}_{ij}\hat{e}^{+,\epsilon}_{ij} + \hat{\lambda}^{\epsilon}_{,\rho_t}(\rho_t)\langle\hat{e}^{\epsilon}_{s}\rangle^{2}_{+}\right)\right\rangle_{+},\\ \hat{\eta}^{\epsilon}_{c}\dot{\rho}_c &= \left\langle \hat{w}^{\epsilon}_{c} - M^{\epsilon}_{c}\frac{\rho_c}{1-\rho_c} - \frac{1}{2}\left(2\hat{\mu}^{\epsilon}_{,\rho_c}(\rho_c)\hat{e}^{-,\epsilon}_{ij}\hat{e}^{-,\epsilon}_{ij}\right)\right\rangle_{+}.\end{aligned} \tag{14}$$

The above expressions are formally equivalent to cf. Frémond and Nedjar (1996, Eq.(23)), with the choice of the damage parameter $\rho_t = 1-\beta_t$ (same for ρ_c).

3. Asymptotic expansions

Given the small thickness of the adhesive, let us set $h^{\epsilon} = \epsilon h$, and look for the solution of the equilibrium problem by using asymptotic expansions method with respect to the small parameter ϵ. In order to perform an asymptotic analysis, it is necessary to transform the ϵ-dependent domain Ω^{ϵ} into a fixed domain Ω through the classical change of coordinates (Ciarlet, 1997), see Fig. 1:

- in the adhesive, the coordinates transformation takes the following form:

$$(x_1,x_2,x_3) \in B^{\epsilon} \to (z_1,z_2,z_3) = (x_1,x_2,\frac{x_3}{\epsilon}) \in B, \tag{15}$$

where $B := \left\{(x_1,x_2,x_3) \in \Omega :\ |x_3| < \frac{h}{2}\right\}$. In addition, given any (scalar or vector) field v defined in B^{ϵ}, it is set $\hat{v}(z_1,z_2,z_3) = v(x_1,x_2,x_3)$;

- In the adherents, the following change of variable is introduced

$$(x_1, x_2, x_3) \in \Omega_{\pm}^{\varepsilon} \to (z_1, z_2, z_3) = (x_1, x_2, x_3 \pm \frac{h}{2} \mp \varepsilon \frac{h}{2}) \in \Omega_{\pm}, \tag{16}$$

where $\Omega_{\pm} := \left\{(x_1, x_2, x_3) \in \Omega : \ \pm x_3 > \frac{h}{2}\right\}$. In addition, given any (scalar or vector) field v defined in $\Omega_{\pm}^{\varepsilon}$, it is set $\bar{v}(z_1, z_2, z_3) = v(x_1, x_2, x_3)$.

The volume and surface forces are supposed to be independent of ε, so that $\mathbf{f}^{\varepsilon}(x_1, x_2, x_3) = \mathbf{f}(z_1, z_2, z_3)$ and $\mathbf{g}^{\varepsilon}(x_1, x_2, x_3) = \mathbf{g}(z_1, z_2, z_3)$. Moreover, according to the change of variables, one has $\frac{\partial}{\partial z_\alpha} = \frac{\partial}{\partial x_\alpha}$ and $\frac{\partial}{\partial z_3} = \varepsilon \frac{\partial}{\partial x_3}$ in B^{ε}.

Finally, we assume that the solution of the equilibrium problem can be written as a series of powers of ε, as follows:

$$\begin{cases} \hat{\boldsymbol{\sigma}}^{\varepsilon} = \hat{\boldsymbol{\sigma}}^0 + \varepsilon\, \hat{\boldsymbol{\sigma}}^1 + o(\varepsilon), \\ \hat{\mathbf{u}}^{\varepsilon} = \hat{\mathbf{u}}^0 + \varepsilon\, \hat{\mathbf{u}}^1 + o(\varepsilon), \\ \bar{\boldsymbol{\sigma}}^{\varepsilon} = \bar{\boldsymbol{\sigma}}^0 + \varepsilon\, \bar{\boldsymbol{\sigma}}^1 + o(\varepsilon), \\ \bar{\mathbf{u}}^{\varepsilon} = \bar{\mathbf{u}}^0 + \varepsilon\, \bar{\mathbf{u}}^1 + o(\varepsilon). \end{cases} \tag{17}$$

By applying the change of coordinate to the governing equation (2), and by injecting (17) into the rescaled problem, the leading term of the asymptotic expansions and its associated limit problem.

3.1. The strain field

The displacement gradient in the rescaled configuration of the adhesive takes the following form:

$$\nabla \hat{\mathbf{u}}^{\varepsilon} = \frac{1}{\varepsilon} \begin{pmatrix} 0 & \hat{u}^0_{\alpha,3} \\ 0 & \hat{u}^0_{3,3} \end{pmatrix} + \begin{pmatrix} \hat{u}^0_{\alpha,\beta} & \hat{u}^1_{\alpha,3} \\ \hat{u}^0_{3,\alpha} & \hat{u}^1_{3,3} \end{pmatrix} + o(\varepsilon). \tag{18}$$

Thus, the strain tensor can be expanded as:

$$\hat{\mathbf{e}}^{\varepsilon} = \frac{1}{\varepsilon} \hat{\mathbf{e}}^{-1} + \hat{\mathbf{e}}^0 + o(\varepsilon), \tag{19}$$

with $\hat{\mathbf{e}}^{-1} := \hat{\mathbf{u}}^0_{,3} \odot \mathbf{e}_3$ and $\hat{\mathbf{e}}^0 := \hat{\mathbf{u}}^0_{,\alpha} \odot \mathbf{e}_\alpha + \hat{\mathbf{u}}^1_{,3} \odot \mathbf{e}_3$. Within the rescaled adherents, the displacement gradient takes the following form:

$$\nabla \bar{\mathbf{u}}^{\varepsilon} = \begin{pmatrix} \bar{u}^0_{\alpha,\beta} & \bar{u}^0_{\alpha,3} \\ \bar{u}^0_{3,\alpha} & \bar{u}^1_{3,3} \end{pmatrix} + o(\varepsilon). \tag{20}$$

Thus, the strain tensor can be expanded as:

$$\bar{\mathbf{e}}^{\varepsilon} = \frac{1}{\varepsilon} \bar{\mathbf{e}}^{-1} + \bar{\mathbf{e}}^0 + o(\varepsilon), \tag{21}$$

with $\bar{\mathbf{e}}^{-1} = \mathbf{0}$ and $\bar{\mathbf{e}}^0 := \bar{\mathbf{u}}^0_{,\alpha} \odot \mathbf{e}_\alpha + \bar{\mathbf{u}}^0_{,3} \odot \mathbf{e}_3$.

3.2. The equilibrium equations

The governing equations (2) can be rewritten in the rescaled configuration. Considering the equilibrium system defined in the adhesive domain, and thanks to the asymptotic development of the stresses (17), one has:

$$0 = \frac{1}{\varepsilon} \hat{\sigma}^{\varepsilon}_{i3,3} + \hat{\sigma}^{\varepsilon}_{i\alpha,\alpha} = \frac{1}{\varepsilon} \hat{\sigma}^0_{i3,3} + \hat{\sigma}^0_{i\alpha,\alpha} + \hat{\sigma}^1_{i3,3} + o(\varepsilon). \tag{22}$$

By identifying the terms with identical power in ε, we get:

$$\hat{\sigma}^0_{i3,3} = 0, \tag{23}$$

and, thus, $\hat{\sigma}^0_{i3}$ is independent of the thickness coordinate z_3. The continuity conditions of the stress vector at the interface leads to:

$$[[\hat{\sigma}^0_{i3}]] = 0, \tag{24}$$

meaning that the jump of the stress vector at $z_3 = \pm\frac{h}{2}$ vanishes.

Considering the rescaled equilibrium equations in the adherents at the lowest order:

$$\bar{\sigma}^0_{ij,j} + f_i = 0 \text{ in } \Omega_{\pm}, \quad \bar{\sigma}^0_{ij} n_j = g_i \text{ on } \Gamma_g. \tag{25}$$

The displacement and stress vector are continuous across the surfaces $S^{\varepsilon}_{\pm}$ and $S_{\pm}$, both in the reference and rescaled configuration, respectively. From the continuity of the displacements, it follows that:

$$\mathbf{u}^{\varepsilon}(\bar{\mathbf{x}}, \pm\varepsilon\frac{h}{2}) = \bar{\mathbf{u}}^{\varepsilon}(\bar{\mathbf{z}}, \pm\frac{h}{2}) = \hat{\mathbf{u}}^{\varepsilon}(\bar{\mathbf{z}}, \pm\frac{h}{2}), \ \bar{\mathbf{x}} = (x_\alpha), \ \bar{\mathbf{z}} = (z_\alpha) \in S. \tag{26}$$

By expanding the displacements in Taylor's series along x_3 and considering (17), one has:

$$\mathbf{u}^\epsilon(\bar{\mathbf{x}}, \pm\varepsilon\frac{h}{2}) = \mathbf{u}^\epsilon(\bar{\mathbf{x}}, 0^\pm) + o(\varepsilon) = \mathbf{u}^0(\bar{\mathbf{x}}, 0^\pm) + o(\varepsilon). \tag{27}$$

By virtue of the continuity conditions, we get:

$$\mathbf{u}^0(\bar{\mathbf{x}}, 0^\pm) + o(\varepsilon) = \bar{\mathbf{u}}^0(\bar{\mathbf{z}}, \pm\frac{h}{2}) + o(\varepsilon) = \hat{\mathbf{u}}^0(\bar{\mathbf{z}}, \pm\frac{h}{2}) + o(\varepsilon), \tag{28}$$

giving

$$\mathbf{u}^0(\bar{\mathbf{x}}, 0^\pm) = \bar{\mathbf{u}}^0(\bar{\mathbf{z}}, \pm\frac{h}{2}) = \hat{\mathbf{u}}^0(\bar{\mathbf{z}}, \pm\frac{h}{2}). \tag{29}$$

Same results are obtained for the stress field. Thus,

$$[\sigma^0_{i3}] = 0, \tag{30}$$

with $[f] := f(\bar{\mathbf{x}}, 0^+) - f(\bar{\mathbf{x}}, 0^-)$ represents the jump across the surface S of f on the limit configuration, as ϵ tends to zero, see Fig. 1(c).

3.3. The constitutive law and damage evolution models

Since the material of the adhesive is assumed to be soft, i.e., mechanically compliant, the elasticity tensor is assumed to be linearly dependent on ε: $\hat{C}^\varepsilon_{ijkl} = \varepsilon\hat{C}_{ijkl}$, and, thus, $\hat{\lambda}^\varepsilon = \varepsilon\hat{\lambda}$ and $\hat{\mu}^\epsilon = \varepsilon\hat{\mu}$. The elastic moduli will depend on one or two damage parameters. Their explicit relation will be explicitly defined in the subsequent sections.

3.3.1. The F1d evolution model

The thermodynamically consistent state and damage evolution laws for the F1d evolution model were derived in Section 2, cf. Eqs. (3)–(8). Considering the adhesive constitutive law (4), at the zero-th order of the asymptotic expansion, it is obtained that

$$\hat{\sigma}^0_{i3} = \hat{C}_{i3j3}(\rho)\hat{u}^0_{j,3} = \hat{\mu}(\rho)\hat{u}^\varepsilon_{i,3} + (\hat{\lambda}(\rho) + \hat{\mu}(\rho))\hat{u}^\varepsilon_{3,3}\delta_{i3}. \tag{31}$$

Since $\hat{\sigma}^0_{i3}$ is independent of z_3, we obtain also that $\hat{u}^0_{i,3}$ does not depend on the thickness coordinate, and thus, $\hat{u}^0_i$ is an affine function of z_3. Moreover, thanks to the continuity conditions at the interface, we get that $\hat{u}^0_{i,3} = \frac{[u^0_i]}{h}$. By substituting the result in (31), we have:

$$\hat{\sigma}^0_{i3} = \frac{1}{h}\hat{C}_{i3j3}(\rho)[u^0_j] = \frac{1}{h}(\hat{\mu}(\rho)[u^0_i] + (\hat{\lambda}(\rho) + \hat{\mu}(\rho))[u^0_3]\delta_{i3}). \tag{32}$$

The constitutive coefficient of the adherents are assumed to be independent of ε, so that $\bar{C}^\varepsilon_{ijkl} = \bar{C}_{ijkl}$. Substituting the expansions of the rescaled displacement and stress into the constitutive equations of the adherents, we obtain the following relations:

$$\bar{\sigma}^0_{ij} = \bar{C}_{ijkl}\bar{e}^0_{kl}.$$

In order to apply the asymptotic expansions method to the damage evolution Eq. (7), let us first compute the negative part $\hat{e}^{-,\varepsilon}_{ij}$ of the strain tensor. Keeping the terms of order $1/\varepsilon$, the rescaled strain tensor in the adhesive takes the following form:

$$\hat{\mathbf{e}}^\epsilon = \frac{1}{\varepsilon}\hat{\mathbf{e}}^{-1} + o(1) = \frac{1}{\varepsilon}\begin{pmatrix} 0 & 0 & \frac{1}{2}\hat{u}^\varepsilon_{1,3} \\ 0 & 0 & \frac{1}{2}\hat{u}^\varepsilon_{2,3} \\ \frac{1}{2}\hat{u}^\varepsilon_{1,3} & \frac{1}{2}\hat{u}^\varepsilon_{2,3} & \hat{u}^\varepsilon_{3,3} \end{pmatrix} + o(1). \tag{33}$$

Let us apply the spectral decomposition to the first approximation of the strain tensor, in order to compute its eigenvalues and the negative part of the tensor (for more details, see Appendix). This entails that

$$\begin{aligned} &\hat{e}^{+,\varepsilon}_{ij}\hat{e}^{+,\varepsilon}_{ij} = \mathrm{Tr}(\hat{\mathbf{e}}^{+,\varepsilon}\hat{\mathbf{e}}^{+,\varepsilon}) \approx \tfrac{1}{\varepsilon^2}\left(\langle\gamma^\varepsilon_+\rangle^2_+ + \langle\gamma^\varepsilon_-\rangle^2_+\right) = \tfrac{1}{\varepsilon^2}(\gamma^\varepsilon_+)^2, \\ &\langle e^\varepsilon_s\rangle^2_+ \approx \tfrac{1}{\varepsilon^2}\langle\hat{u}^\varepsilon_{3,3}\rangle^2_+, \end{aligned} \tag{34}$$

where $\gamma^\varepsilon_\pm := \frac{1}{2}\left(\hat{u}^\varepsilon_{3,3} \pm |\hat{\mathbf{u}}^\varepsilon_{,3}|\right)$, $|\hat{\mathbf{u}}^\epsilon_{,3}| := \sqrt{(\hat{u}^\varepsilon_{1,3})^2 + (\hat{u}^\varepsilon_{2,3})^2 + (\hat{u}^\varepsilon_{3,3})^2}$, are two eigenvalues. Since $\gamma^\varepsilon_+ \geq 0$ and $\gamma^\varepsilon_- \leq 0$, we obtain that $\langle\gamma^\varepsilon_-\rangle_+ = 0$ e $\langle\gamma^\varepsilon_+\rangle_+ = \gamma^\varepsilon_+$. Note that, in general, $\langle f + g\rangle_+ \neq \langle f\rangle_+ + \langle g\rangle_+$, i.e., the negative part of a function is not linear operator and, thus, cannot be distributed on the sum. However, as a first approximation of the asymptotic procedure, we can retain the lowest terms of order $1/\varepsilon$, that is, $\langle\frac{1}{\varepsilon}\hat{u}^\varepsilon_{3,3} + o(1)\rangle_+$, and neglect the higher-order terms.

Let us rescale Eqs. (7), with the assumptions that $\hat{\omega}^\epsilon(\rho) = \frac{1}{\varepsilon}\hat{\omega}(\rho)$, $\hat{\eta}^\epsilon = \frac{1}{\varepsilon}\hat{\eta}$, $\hat{\lambda}^\varepsilon = \varepsilon\hat{\lambda}$ and $\hat{\mu}^\epsilon = \varepsilon\hat{\mu}$, keeping the terms at order $1/\varepsilon$, see Bonetti et al. (2017):

$$\hat{\eta}\dot{\rho} = \left\langle\hat{\omega}_{,\rho}(\rho) - \tfrac{1}{2}\left(2\hat{\mu}_{,\rho}(\rho)(\gamma^\varepsilon_+)^2 + \hat{\lambda}_{,\rho}(\rho)\langle\hat{u}^\varepsilon_{3,3}\rangle^2_+\right)\right\rangle_+ + o(1), \tag{35}$$

Then, by considering the asymptotic expansion of the unknowns, truncating the power series at the zero-th order and by using the matching conditions, together with the results obtained the first part of this section, we get:

$$\hat{\eta}\dot{\rho} = \left\langle\hat{\omega}_{,\rho}(\rho) - \tfrac{1}{2\hat{h}^2}\left(2\hat{\mu}_{,\rho}(\rho)(\gamma^0_+)^2 + \hat{\lambda}_{,\rho}(\rho)\langle[u^0_3]\rangle^2_+\right)\right\rangle_+, \tag{36}$$

where $\gamma^0_\pm := \frac{1}{2}\left([u^0_3] \pm |[\mathbf{u}^0]|\right)$, with $|[\mathbf{u}^0]| := \sqrt{[u^0_1]^2 + [u^0_2]^2 + [u^0_3]^2}$.

3.3.2. The F2d evolution model

The thermodynamically consistent state and damage evolution laws for the F1d evolution model were derived in Section 2, cf. Eqs. (9)–(14). Considering the adhesive constitutive law (11), at the zero-th order of the asymptotic expansion, it is obtained that

$$\hat{\sigma}^0_{i3} = \hat{C}_{i3j3}(\rho_t)(\hat{e}^{-1}_{j3})^+ - \hat{C}_{i3j3}(\rho_c)(\hat{e}^{-1}_{j3})^-, \tag{37}$$

where $(\hat{e}^{-1}_{j3})^\pm$ denote the components of the positive and negative parts of tensor $(\hat{e}^{-1}_{j3})$. Component-wise, by means of the spectral decomposition described in Appendix, it is possible to write:

$$\begin{aligned}
\hat{\sigma}^0_{\alpha 3} &= \tfrac{1}{2}(\hat{\mu}(\rho_t)+\hat{\mu}(\rho_c))\hat{u}^0_{\alpha,3} + \tfrac{1}{2}(\hat{\mu}(\rho_t)-\hat{\mu}(\rho_c))\tfrac{\hat{u}^0_{\alpha,3}\hat{u}^0_{3,3}}{|\hat{\mathbf{u}}^0_{,3}|},\\
\hat{\sigma}^0_{33} &= \tfrac{1}{2}(\hat{\kappa}(\rho_t)+\hat{\kappa}(\rho_c))\hat{u}^0_{3,3} + \tfrac{1}{4}(\hat{\kappa}(\rho_t)-\hat{\kappa}(\rho_c))\left(|\hat{\mathbf{u}}^0_{,3}| + \tfrac{(\hat{u}^0_{3,3})^2}{|\hat{\mathbf{u}}^0_{,3}|}\right),
\end{aligned} \tag{38}$$

with $\hat{\kappa} := \hat{\lambda} + 2\hat{\mu}$. Since Eqs. (38) must be satisfied for arbitrary values of the Lamé's constants, and by means of the independence of $\hat{\sigma}^0_{i3}$ with respect to z_3, it is possible to infer that quantities $\hat{u}^0_{i,3}$, $\frac{\hat{u}^0_{\alpha,3}\hat{u}^0_{3,3}}{|\hat{\mathbf{u}}^0_{,3}|}$ and $|\hat{\mathbf{u}}^0_{,3}| + \frac{(\hat{u}^0_{3,3})^2}{|\hat{\mathbf{u}}^0_{,3}|}$ are also constant in z_3. Thus, $\hat{u}^0_i$ are affine functions of z_3, and, by virtue of the continuity conditions at the top and bottom interfaces with the adherents, $\hat{u}^0_{i,3} = \frac{[u^0_i]}{h}$. By substituting the jumps of the displacements into expression (38), one has:

$$\begin{aligned}
\hat{\sigma}^0_{\alpha 3} &= \tfrac{1}{2h}(\hat{\mu}(\rho_t)+\hat{\mu}(\rho_c))[u^0_\alpha] + \tfrac{1}{2h}(\hat{\mu}(\rho_t)-\hat{\mu}(\rho_c))\tfrac{[u^0_\alpha][u^0_3]}{|[\mathbf{u}^0]|},\\
\hat{\sigma}^0_{33} &= \tfrac{1}{2h}(\hat{\kappa}(\rho_t)+\hat{\kappa}(\rho_c))[u^0_3] + \tfrac{1}{4h}(\hat{\kappa}(\rho_t)-\hat{\kappa}(\rho_c))\left(|[\mathbf{u}^0]| + \tfrac{[u^0_3]^2}{|[\mathbf{u}^0]|}\right).
\end{aligned} \tag{39}$$

Note that when $\rho_t = \rho_c := \rho$, $\hat{\sigma}^0_{\alpha 3} = \frac{1}{h}\hat{\mu}(\rho)[u^0_\alpha]$ and $\hat{\sigma}^0_{33} = \frac{1}{h}\hat{\kappa}(\rho)[u^0_3]$, and, thus, the classical spring-type conditions are recovered, see Bonetti et al. (2017). It is worth mentioning, that the above interface transmission conditions are non linear with respect to the displacement jumps.

By rescaling (13) and applying the same arguments adopted for the F1d damage evolution model, we obtain:

$$\begin{aligned}
\hat{\eta}_t\dot{\rho}_t &= \left\langle \hat{\omega}_{t,\rho_t}(\rho_t) - \tfrac{1}{2h^2}\left(2\hat{\mu}_{,\rho_t}(\rho_t)(\gamma^0_+)^2 + \hat{\lambda}_{,\rho_t}(\rho_t)\langle[u^0_3]\rangle^2_+\right)\right\rangle_+,\\
\hat{\eta}_c\dot{\rho}_c &= \left\langle \hat{\omega}_{c,\rho_c}(\rho_c) - \tfrac{1}{h^2}\hat{\mu}_{,\rho_c}(\rho_c)(\gamma^0_-)^2\right\rangle_+.
\end{aligned} \tag{40}$$

4. A benchmark numerical example

In this Section, we present the numerical application of the two aforementioned damage evolution models to a composite structure, consisting of two adherents bonded by an adhesive layer that can undergo damage. The composite's equilibrium response under axial loading is analyzed in order to evaluate the behavior predicted by each damage model. For the sake of brevity and considering the results of the asymptotic analysis at the lowest order (e.g. the zero-th order), the apex "0" from the previous notation for the stress, strain and displacement components is omitted. In the following, the index "0" will be used to denote the values of the material parameters before damage.

The adherents are modeled as two identical, isotropic elastic blocks, denoted $\Omega_\pm$, of common length L and height $H_\pm$, as depicted in Fig. 2. The adhesive's thickness is denoted by h, so that the total height of the composite is $H_{tot} = H_+ + H_- + h$. In the case of a soft device, uniform normal distributed forces of intensity q_3, respectively, are applied to the boundaries of the two blocks and body forces are neglected. In the case of a hard device, relative normal displacements are applied to the upper and lower bases of the composite, and q_3 are distributed reaction forces.

In the two adherents, the stress tensor is assumed to take the simple form

$$\bar{\sigma} = q_3\,(\mathbf{e}_3 \otimes \mathbf{e}_3), \tag{41}$$

with $\mathbf{e}_3$ the unit vector of the 3-axis. This particular choice of stress distribution ensures that the transmission conditions (24) and the equilibrium equations (25) are automatically satisfied. The adherents are assumed to be composed of isotropic linear elastic materials with elasticity parameters E, ν.

Let $\bar{\mathbf{u}}_\pm$ be the displacement field in the upper (lower) block. The constitutive equations in the two adherents and compatibility with the adhesive require that

$$\bar{\mathbf{u}}_\pm(\mathbf{x}) = \left(-\frac{\nu\, q_3}{E}x_1 \pm \frac{[u_1]}{2}\right)\mathbf{e}_1 + \left(-\frac{\nu\, q_3}{E}x_2 \pm \frac{[u_2]}{2}\right)\mathbf{e}_2 + \left(\frac{q_3}{E}x_3 \pm \frac{[u_3]}{2}\right)\mathbf{e}_3, \quad \mathbf{x} \in \Omega_\pm, \tag{42}$$

where $[u_i]$ denote the displacement jumps across the adhesive limit surface S. These jumps account for the adhesive's deformation and depend on the particular damage model (F1d or F2d).

The mechanical behavior of the composite block is given by its force–displacement response $F - D$, where

$$D := (\bar{\mathbf{u}}_+(x_1, x_2, H_+ + h/2) - \bar{\mathbf{u}}_-(x_1, x_2, -H_- - h/2)) \cdot \mathbf{e}_3 \tag{43}$$

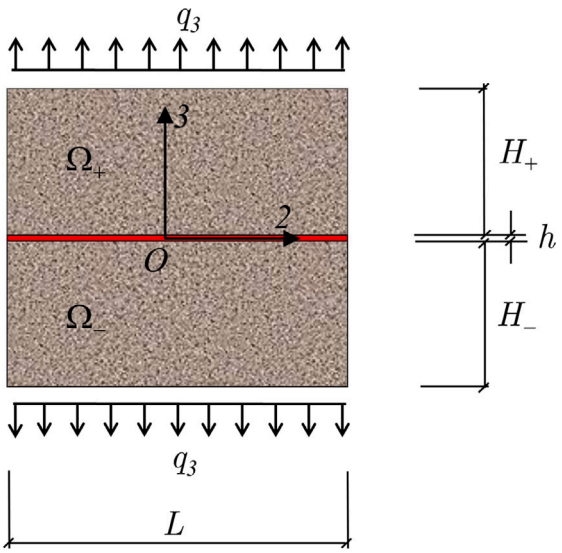

Fig. 2. Geometric configuration and applied loads for a composite, made of two adherent blocks joined by a damaging adhesive, and subjected to uniform normal load.

is the macroscopic normal displacement, and the macroscopic force is

$$F(t) = q_3 A, \tag{44}$$

with A the bonded area. Using Eqs. (42) and (43), the jump $[u_3]$ can be related to the force F and to the macroscopic normal displacement D as follows:

$$[u_3] = D - \frac{F}{EA} H_{tot}. \tag{45}$$

In the case of soft device, F is prescribed, while in the case of hard device D is prescribed.

4.1. Explicit forms of damage-dependent moduli from micromechanical schemes

The soft, isotropic elastic adhesive joining the adherent can undergo damage. To model the softening behavior of the adhesive when damaged, the damage parameter ρ is identified by the porosity of the medium, defined as the volume fraction of pores. In particular, two different modeling approaches are adopted to link the macroscopic softening of the material to the porosity. The first is the Kachanov-Sevostianov (KS) micromechanical homogenization scheme, which relies on the approximation of non-interacting microvoids (Kachanov, 1994; Kachanov & Sevostianov, 2018; Kachanov et al., 1994; Pronina et al., 2025). The second is the approximated Mori–Tanaka-Benveniste (MTB) scheme, which accounts for the effect of pore interactions on the overall elastic properties (Benveniste, 1986; Mori & Tanaka, 1973; Stefaniuk & Kachanov, 2024).

According to the KS scheme, for a random distribution of spheroidal voids in a linear elastic isotropic matrix, the following structure for the effective Young's modulus $\hat{E}_{KS}(\rho)$ and shear modulus $\hat{G}_{KS}(\rho)$ emerges:

$$\begin{aligned} \hat{E}_{KS}(\rho) &= \frac{\hat{E}_0}{(1 + C_E\,\rho)}, \\ \hat{G}_{KS}(\rho) &= \frac{\hat{G}_0}{(1 + C_G\,\rho)}, \end{aligned} \tag{46}$$

where $\hat{E}_0, \hat{G}_0$ are the initial elasticity parameters of the undamaged adhesive, and C_E, C_G are shape factors, depending on the particular distribution of defects, see Kachanov and Sevostianov (2018) and Pronina et al. (2025). The corresponding Lamé's parameter are

$$\hat{\lambda}_{KS}(\rho) = \hat{G}_{KS}(\rho)\frac{\xi - 2 + (\xi C_G - 2C_E)\rho}{3 - \xi + (3C_E - \xi C_G)\rho}, \tag{47}$$

$$\hat{\mu}_{KS}(\rho) = \hat{G}_{KS}(\rho), \tag{48}$$

with $\xi := \hat{E}_0/\hat{G}_0$.

The MTB micromechanical scheme introduces the inhomogeneities into the average stress over the matrix, that may differ from the stress applied remotely. Porosity increases the average stress in the matrix by a factor of $1/(1-\rho)$, thereby increasing its strain

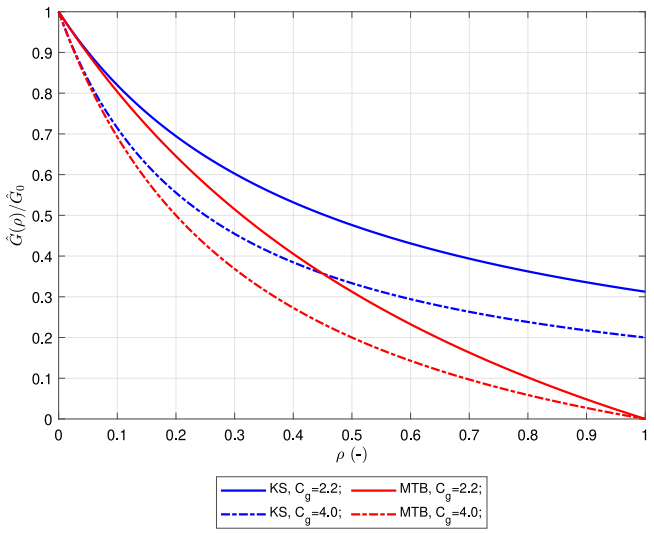

Fig. 3. Normalized effective shear modulus as a function of damage for KS and MTB micromechanical descriptions, shown for two different values of the shape factor C_G..

contribution. This gives for the effective Young's modulus $\hat{E}_{MTB}(\rho)$ and shear modulus $\hat{G}_{MTB}(\rho)$ the following expressions:

$$\hat{E}_{MTB}(\rho) = \frac{\hat{E}_0}{(1 + C_E\ \rho/(1-\rho))}, \qquad \hat{G}_{MTB}(\rho) = \frac{\hat{G}_0}{(1 + C_G\ \rho/(1-\rho))}, \tag{49}$$

where $\hat{E}_0, \hat{G}_0$ are again the initial elasticity parameters, and C_E, C_G shape factors. The corresponding Lamé's parameter are

$$\hat{\lambda}_{MTB}(\rho) = \hat{G}_{MTB}(\rho)\frac{\xi - 2 + (\xi C_G - 2C_E)\rho/(1-\rho)}{3 - \xi + (3C_E - \xi C_G)\rho/(1-\rho)}, \tag{50}$$

$$\hat{\mu}_{MTB}(\rho) = \hat{G}_{MTB}(\rho). \tag{51}$$

These explicit functions for $\hat{\mu}(\rho)$ and $\hat{\lambda}(\rho)$, along with their derivatives $\hat{\mu}_{,\rho}$ and $\hat{\lambda}_{,\rho}$, couple the micromechanical descriptions to the damage evolution laws (36) and (40) derived in Section 3.3.

Fig. 3 illustrates the degradation of the normalized effective shear modulus, $\hat{G}(\rho)/\hat{G}_0$ as a function of the damage parameter ρ for both the KS and MTB micromechanical schemes. Two values for the shape factor, $C_G = 2.2$ and $C_G = 4.0$, are considered to demonstrate its influence. For any given value of shape factor, the MTB model consistently predicts a more rapid degradation of the effective modulus with increasing damage compared to the KS model. At higher damage levels, the $\rho/(1-\rho)$ term in the MTB formulation leads to a significant decrease in stiffness, driving the effective modulus to zero as ρ approaches unity. In contrast, the KS model shows a more gradual decline and retains a non-zero modulus ($\hat{G}(\rho)/\hat{G}_0 = 1/(1+C_G)$) even at damage values approaching $\rho = 1$. For both KS and MTB schemes, increasing the shape factor C_G results in a faster rate of shear modulus degradation. This implies that the same level of damage ρ has a more detrimental effect on the material's effective stiffness.

4.2. The F1d evolution model

In the F1d model, the adhesive behavior is modeled as an imperfect interface governed by the transmission conditions (32) and by the damage evolution equation (36). Substituting the stress representation (41) into the transmission conditions (32) and the damage evolution equation (36), we obtain the conditions $[u_1] = 0$ and $[u_2] = 0$ and the following differential–algebraic system of equations:

$$q_3 = (2\hat{\mu}(\rho) + \hat{\lambda}(\rho))\frac{[u_3]}{h}, \tag{52}$$

$$\hat{\eta}\dot{\rho} = \left\langle \hat{w} - \frac{(2\hat{\mu}_{,\rho}(\rho) + \hat{\lambda}_{,\rho}(\rho))}{2h^2}\langle [u_3]\rangle_+^2 \right\rangle_+, \tag{53}$$

assuming $\hat{\omega}(\rho) := \hat{w}\rho$, for simplicity. In (53), the last term within Macauley's brackets vanishes in compression, thereby distinguishing between the cases of traction and compression.

Table 1
Geometrical, material, and loading parameters used in the numerical simulations.

	Quantity	Symbol	Value		Unit
			Figs. 4–10	Fig. 11	
Geometry	Adherents' height	$H_{\pm}$	50.00[a]	24.50[f]	mm
	Adhesive's thickness	h	1.00[b]	0.39[f]	mm
	Bonded section area	A	400 × 100[a]	644.03[f,g]	mm^2
Adherents	Young's modulus	E	38.00[a]	210.00[f]	GPa
	Poisson's ratio	ν	0.20[a]	0.30[f]	–
Adhesive	Undamaged Young's modulus	$\hat{E}_0$	0.342[c]	3.28[f]	GPa
	Undamaged shear modulus	$\hat{G}_0$	0.120[c]	1.20[f]	GPa
	Damage rate Coeff.	$\hat{\eta}_{t,c}$	0.072[a]	15.00[h]	MPa s
	Damage threshold	$\hat{w}_{t,c}$	0.011[a]	See note[i]	MPa
	Shape factor	C_E	2.20[e]	2.20[e]	–
	Shape factor	C_G	2.20[e]	2.20[e]	–
	Initial damage	ρ_0	0[d]	0[d]	–
Loading device	Loading rate	$\dot{F}$	10[d]	0.9[j]	kN/s
	Displacement rate	$\dot{D}$	1[d]	–	mm/s

[a] Value based on the study by Freddi and Frémond (2006).
[b] Value assumed for consistency with the thin-layer assumption of the interface model.
[c] Value typical of a structural adhesive, cf. Technical (0000).
[d] Assumed value for illustrative virtual tests.
[e] Value corresponding to a collective of randomly oriented prolate spheroidal pores, cf. Pronina et al. (2025, Fig. 1).
[f] Value based on the experimental work by Adams and Coppendale (1976, 1979).
[g] Calculated from reported inner (36 mm) and outer (46 mm) diameters (Adams & Coppendale, 1976).
[h] Value chosen to give a good qualitative fit to the experimental data; assumed $\hat{\eta} = \hat{\eta}_t = \hat{\eta}_c$.
[i] Values chosen for good qualitative fit: $\hat{w}_t = 0.0365$ MPa (KS), $\hat{w}_t = 0.8$ MPa (MTB), and $\hat{w}_c = 30$ MPa (for both schemes).
[j] Assumed quasistatic loading rate for the soft device simulation.

4.3. The F2d evolution model

In the F2d model, the transmission conditions (39) together with the damage evolution Eq. (40) govern the damaging adhesive behavior. Substituting Eq. (41) into Eqs. (39) and (40), we obtain the conditions $[u_1] = 0$ and $[u_2] = 0$ and the following differential–algebraic system of equations:

$$q_3 = \frac{\hat{\kappa}(\rho_t)}{h}\langle [u_3]\rangle_+ + \frac{\hat{\kappa}(\rho_c)}{h}\langle [u_3]\rangle_-, \tag{54}$$

$$\hat{\eta}_t \dot{\rho}_t = \left\langle \hat{w}_t - \frac{(2\hat{\mu}_{,\rho_t}(\rho_t) + \hat{\lambda}_{,\rho_t}(\rho_t))}{2h^2}\langle [u_3]\rangle_+^2 \right\rangle_+, \tag{55}$$

$$\hat{\eta}_c \dot{\rho}_c = \left\langle \hat{w}_c - \frac{\hat{\mu}_{,\rho_c}(\rho_c)}{h^2}\langle [u_3]\rangle_-^2 \right\rangle_+, \tag{56}$$

where we have assumed $\hat{\omega}_t(\rho_t) := \hat{w}_t\ \rho_t$, and $\hat{\omega}_t(\rho_c) := \hat{w}_c\ \rho_c$, for simplicity. Notably, in the simple case of axial loading considered here, the interface transmission condition (54) becomes linear with respect to the displacement jumps. In the evolution equations (55) and (56), the presence of the Macauley's brackets distinguish between the cases of traction and compression.

4.4. Numerical results

In this Subsection, the coupled differential–algebraic problems of the two models, F1d and F2d, governing the adhesive's response are solved numerically to illustrate its damaging behavior under the KS and MTB micromechanical schemes. The geometrical and initial material properties of the adherents and the adhesive are chosen to simulate a realistic case and are detailed in Table 1. The chosen values of the geometrical and material parameters ensure that damage evolution and failure occur within a simulated timeframe of 50 s and that the differences between the model formulations are observable.

Simulations of tensile-compression tests are performed in the cases of hard and soft devices. In the simulations for a hard device, the overall normal displacement D is prescribed as follows:

$$D = \dot{D}t, \tag{57}$$

where t is the time and $\dot{\delta}$ is given in Table 1. In the simulations for a soft device, the distributed normal force F is prescribed as follows:

$$F = \dot{F}t, \tag{58}$$

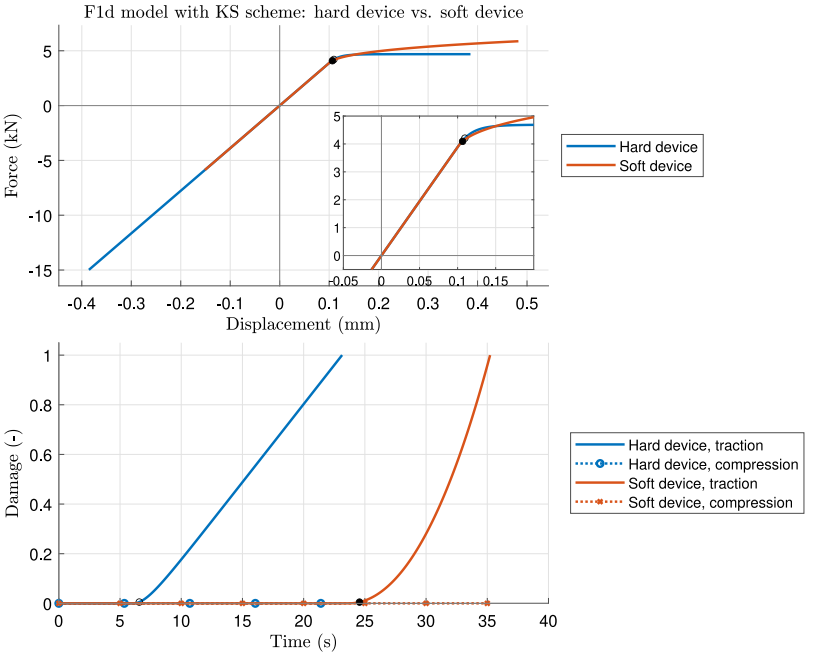

Fig. 4. Force–displacement responses (top panel) and damage evolutions (bottom panel) for the F1d model with the KS micromechanical scheme, considering hard and soft loading device.

where $\dot{F}$ is given in Table 1.

For the F1d evolution model, the problem is governed by Eqs. (52), (53), (47), (48), with the initial condition $\rho(0) = \rho_0$. For all simulations presented, the initial damage is assumed to be zero, i.e., $\rho_0 = 0$.

For the F2d evolution model, the problem is governed by the system of differential–algebraic of equations (DAEs) (54)–(56), together with (47), (48), and the initial condition $\rho(0) = \rho_0$.

We performed simulations for each micromechanical scheme (KS and MTB), considering four cases: two loading cases (soft and hard devices) and two damage models (F1d and F2d). For each case, the governing system of first-order differential–algebraic of equations (DAEs) is solved numerically in MATLAB (2024) using the *ode15s* solver, implementing a dedicated differential–algebraic function. Null initial conditions were set for the state vector (ρ, F) or (ρ, D) for the F1d model, and (ρ_t, ρ_c, F) or (ρ_t, ρ_c, D) for the F2d model, representing an initially undamaged state with zero initial stresses and consistent with zero initial applied global strains. Relative and absolute error tolerances for the solver were set to 10^{-4} and 10^{-6}, respectively. To assist the solver in identify consistent initial conditions for the DAE system, the *InitialSlope* option was set to a zero vector.

4.4.1. Joint's response for the F1d model

In the following section the numerical results of the F1d model are presented. Fig. 4 illustrates the force–displacement $(F - D)$ and damage-time response of the joint for the F1d model using the KS micromechanical scheme. The top panel of the Figure shows the macroscopic force–displacement responses of the F1d damage model when using hard and soft loading devices. As expected, both responses exhibit identical initial elastic stiffness since they share the same undamaged adhesive material properties $(\hat{E}_0, \hat{\nu}_0)$ and adherent material properties. Damage initiation, marked at $\rho = 0.005$ by open circles for the hard device and filled circles for the soft device, occurs slightly earlier for the soft device. After damage initiation, the curve for the hard device displays a ductile plateau while the curve for the soft device exhibits a slightly ascending branch until complete damage is reached, which occurs at lower force and displacement levels for the hard device. The force–displacement response in compression is linear elastic for both loading devices. A notable tension–compression asymmetry is observed for the hard device, with normal compressive forces far exceeding tensile ones. This is due to the term within Macauley's brackets in the damage law (53), whose deactivation under compression slows down the damaging process. The damage evolution plots, shown in the bottom panel of Fig. 4, further explain the mechanical responses. In traction, adhesive damage occurs rapidly, reaching full damage ($\rho = 1$) more quickly in the hard loading device. In compression, the term within Macauley's brackets in Eq. (53) vanishes, deactivating the damage, which remains constant at the initial zero value. This causes the linear elastic response.

Fig. 5 shows the response of the joint for the F1d model with the MTB micromechanical scheme. In traction, the response after the onset of damage is qualitatively different compared to the KS scheme. Hard device simulation demonstrates stable post-peak softening, whereby the reaction force decreases as the material's stiffness degrades due to damage, enabling the entire failure process to be traced. By contrast, the soft device exhibits unstable, catastrophic failure at the critical time $t \approx 28.7$ s, corresponding to a finite-time singularity in the DAE system. Indeed, as damage accumulates, the adhesive's stiffness decreases. This requires a

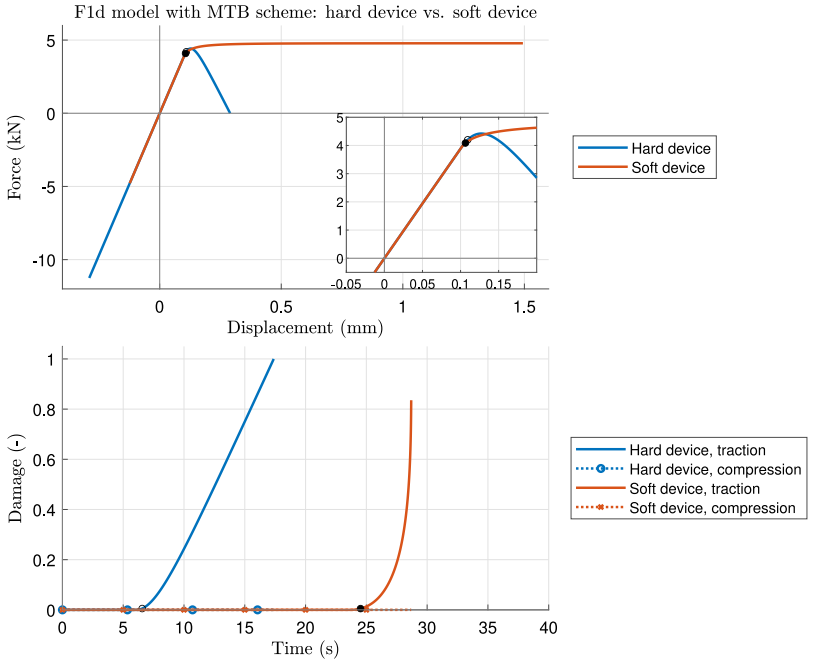

Fig. 5. Force–displacement responses (top panel) and damage evolutions (bottom panel) for the F1d model with the MTB micromechanical scheme, considering hard and soft loading device.

rapid increasing displacement to withstand the prescribed load. This larger displacement, in turn, accelerates the rate at which the damage evolves. The resulting positive feedback loop causes a finite-time singularity in the governing equations, where the damage parameter ρ_t and the displacement D approach infinity. The *ode15s* solver's inability to proceed beyond this point correctly identifies the critical time of structural collapse. Under compression, the response of the system is linear elastic, due again to the deactivation of the damage parameter caused by the term within Macauley's brackets in Eq. (53).

The tension–compression asymmetry, characterized by high compressive strength and a lower softening tensile response, as predicted by the F1d model in the MTB case, is consistent with experimental observations on axially loaded butt joints composed of steel adherends joined with BSL 308 A film adhesive, as studied by Adams and Coppendale (1979, Figure 6). They measured a peak tensile stress of approximately 75 MPa for the butt joint, which sustained compressive stresses of over 300 MPa before failing. Their results also show a softening behavior in traction and a nearly linear response in compression, trends which are well-captured by our model. This qualitative agreement preliminarily verifies the model's physical plausibility and demonstrates its potential to accurately represent real material responses.

4.4.2. Joint's response for the F2d model

A main feature of the F2d damage model is the different description of damage nucleation and evolution in traction and compression regulated by the damage thresholds $\hat{w}_t, \hat{w}_c$, and damage rate coefficients $\hat{\eta}_t, \hat{\eta}_c$, respectively. At this stage, to demonstrate the F2d model's capability to represent different material behaviors by varying the relative values of these parameters, two cases were considered for both micromechanical schemes KS and MTB:

- Case (a): the damage thresholds and damage rate coefficients $\hat{w}_t, \hat{w}_c$, and $\hat{\eta}_t, \hat{\eta}_c$, are identical for tensile and compressive modes. In particular, $\hat{w}_t = \hat{w}_c = \hat{w}$, and $\hat{\eta}_t = \hat{\eta}_c = \hat{\eta}$, with $\hat{w}$ and $\hat{\eta}$, see Table 1.
- Case (b): the tensile parameters were reduced of a factor 10, i.e. $\hat{w}_t = \hat{w}/10$, $\hat{\eta}_t = \hat{\eta}/10$, while the compression parameters were left unmodified, i.e. $\hat{w}_c = \hat{w}$, $\hat{\eta}_c = \hat{\eta}$.

For case (a) in hard and soft devices, the macroscopic force–displacement responses is shown in 6 and in Fig. 7 for the schemes KS and MTB, respectively. Even with these symmetric material parameters, a significant tension–compression asymmetry is observed, with a ductile behavior both in traction and in compression. This is due to the fact that the damage parameter for tension, ρ_t, evolves only in traction and the damage parameter for compression, ρ_c, evolves only in compression, as shown in the middle and bottom panels of Fig. 6. The tensile force–displacement curve was stopped when $\rho_t = 1$, and the compressive force–displacement curve when $\rho_c = 1$. Moreover, the evolutions of ρ_t and ρ_c are regulated differently by the differential equations (55) and (56) due to the presence of the positive and negative parts of the jump, and the different elasticity coefficients involved ($2\hat{\mu}_{,\rho_t} + \hat{\lambda}_{,\rho_t}$ vs. $\hat{\mu}_{,\rho_t}$). These differences leads to earlier damage initiation for ρ_t in traction, see the middle and bottom panels of Fig. 6, as well as lower force and displacement values at full damage compared to compression. With the KS micromechanical scheme, the force–displacement

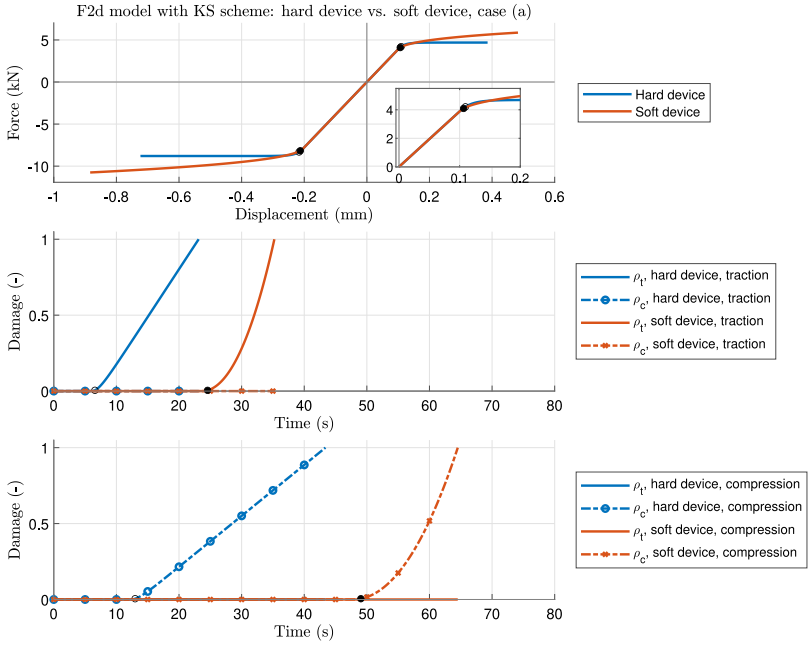

Fig. 6. Case (a): force–displacement responses (top panel) and damage evolutions under traction and compression (middle and bottom panels, respectively) for the F2d model with the KS micromechanical scheme, considering hard and soft loading device.

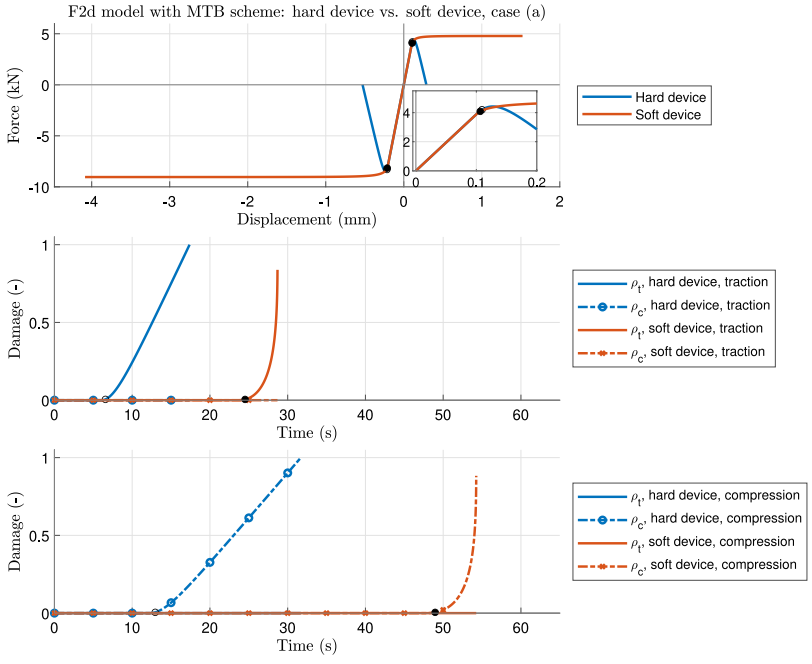

Fig. 7. Case (a): force–displacement responses (top panel) and damage evolutions under traction and compression (middle and bottom panels, respectively) for the F2d model with the MTB micromechanical scheme, considering hard and soft loading device.

curve for the hard device shows a ductile plateau immediately after damage initiation, whereas the curve for the soft device shows an ascending branch until complete damage occurs. The micromechanical MTB scheme produces a more complex response. Under displacement control (hard device), a stable post-peak softening response occurs both in traction and in compression: the reaction force (F) decreases as the material's stiffness degrades due to damage. Under loading control (soft device), finite-time singularities at $t \approx 28.7$ s and $t \approx 54.2$ s occur in traction and in compression, respectively, corresponding to catastrophic failure of the joint.

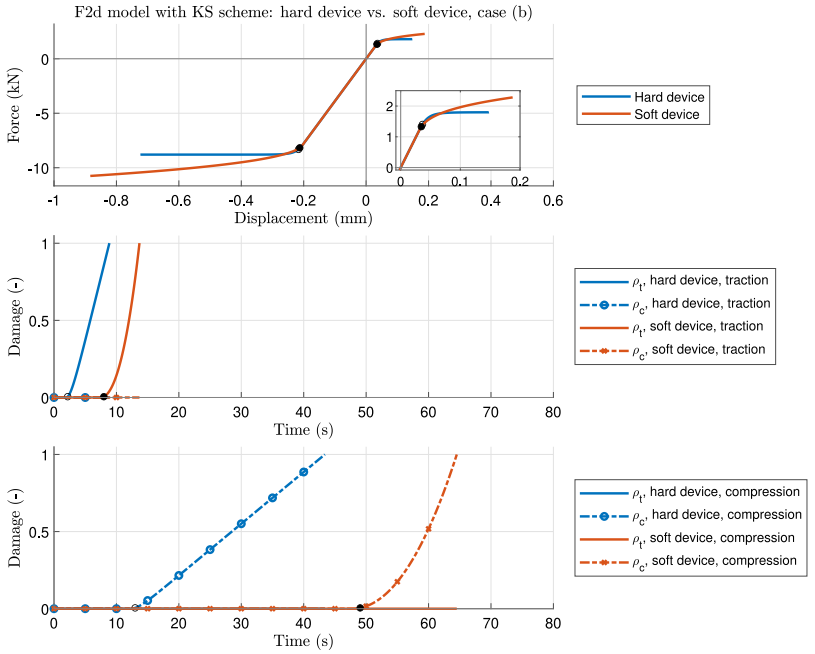

Fig. 8. Case (b): force–displacement responses (top panel) and damage evolutions under traction and compression (middle and bottom panels, respectively) for the F2d model with the KS micromechanical scheme, considering hard and soft loading device.

In case (b), illustrated in Figs. 8 and 9 for the KS and MTB schemes, respectively, the material is assumed to be more susceptible to tensile damage. This is achieved by reducing both the tensile damage threshold, $\hat{w}_t = \hat{w}/10$, and the tensile damage rate coefficient, $\hat{\eta}_t = \hat{\eta}/10$, relative to their compressive counterparts, $\hat{w}_c = \hat{w}$, $\hat{\eta}_c = \hat{\eta}$, where $\hat{w}$ and $\hat{\eta}$ are the baseline values from Table 1. As expected, these parameters' modification leads to earlier damage initiation for ρ_t under traction, as shown by its evolution represented in middle panel of Fig. 8. Correspondingly, for both micromechanical schemes, the maximum tensile force is substantially lower compared to case (a) and failure now occurs at much smaller displacements. Also in this case, the MTB schemes produces softening under displacement control and catastrophic failure under loading control at times $t \approx 10.6$ s in traction and $t \approx 54.2$ s in compression. The compressive response is similar to case (a).

Fig. 10 illustrates the dependence of the maximum force, F_{max}, and the damage onset time, t_o, on the traction damage rate coefficient, η_t, and the traction damage threshold, ω_t, during uniaxial traction for the two micromechanical schemes (KS and MTB) and the two loading devices (hard and soft). The top-left panel shows that F_{max} increases with increasing values of η_t in all cases. Higher values of η_t delay damage evolution, enabling the joint to withstand greater stresses before failing. Force control (soft device, pink/red curves) consistently allows for higher peak forces than displacement control (hard device, blue curves). In this regime, the KS model (solid lines) predicts greater strength than the MTB model (dashed lines). The top-right panel shows that F_{max} depends strongly on the damage threshold ω_t, increasing significantly as the threshold for damage initiation rises. The responses for the two loading devices and the two micromechanical schemes are nearly identical, indicating that the peak force is primarily governed by the damage threshold and is largely independent of the loading type or micromechanical model for this loading path. The bottom panels show the time to damage onset, t_o. As expected, t_o increases with both η_t and ω_t, as these parameters increase the resistance of the material to damage. Force control results in a significantly longer time to damage initiation than displacement control for any given set of damage parameters. As the maximum force, F_{max}, and the damage onset time, t_o, during uniaxial compression exhibit similar trends with respect to the compression damage rate coefficient, η_c, and the compression damage threshold, ω_c, they are not reported here.

4.5. Comparison with experimental results

To verify the physical plausibility of the models, their predictions were compared with the classic experimental data for axially loaded adhesive butt joints reported by Adams and Coppendale (1979). In their study, butt joints were fabricated using EN 25 steel adherents and BSL 308 A film adhesive. The digitized stress–strain curve from their results was obtained using WebPlotDigitizer (Rohatgi, 2024) and it is presented in Fig. 11. This figure also shows the stress–strain curves predicted by the F1d and F2d models, which use the geometric and material parameters listed in Table 1. In the case of pure uniaxial tension, the compressive damage variable ρ_c in the F2d model is not activated. Consequently, the F2d model governing equations reduce to those of the F1d model. For this reason, the predicted curves for the F1d and F2d models coincide for each micromechanical scheme. The results show strong qualitative agreement with the experimental data. Models based on the KS scheme predict initial

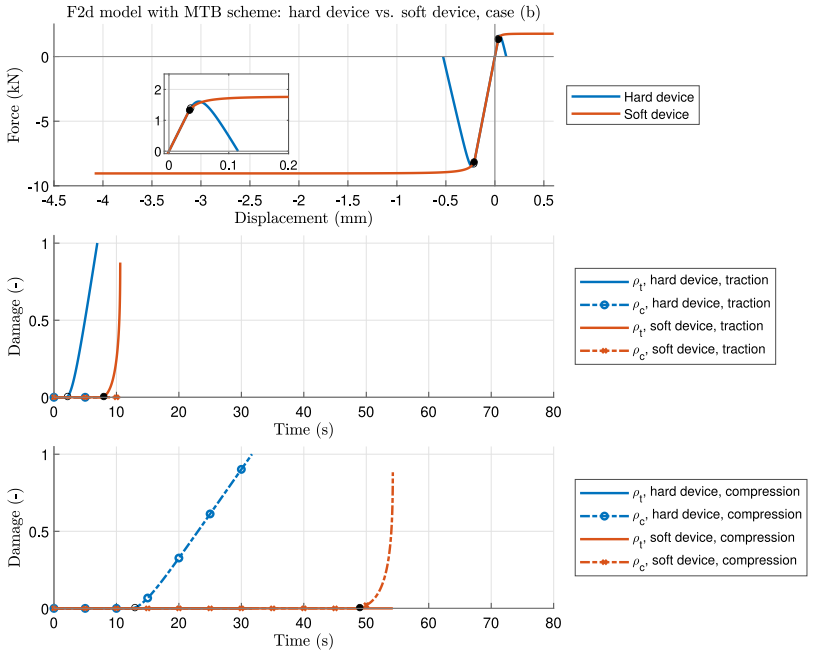

Fig. 9. Case (b): force–displacement responses (top panel) and damage evolutions under traction and compression (middle and bottom panels, respectively) for the F2d model with the MTB micromechanical scheme, considering hard and soft loading device.

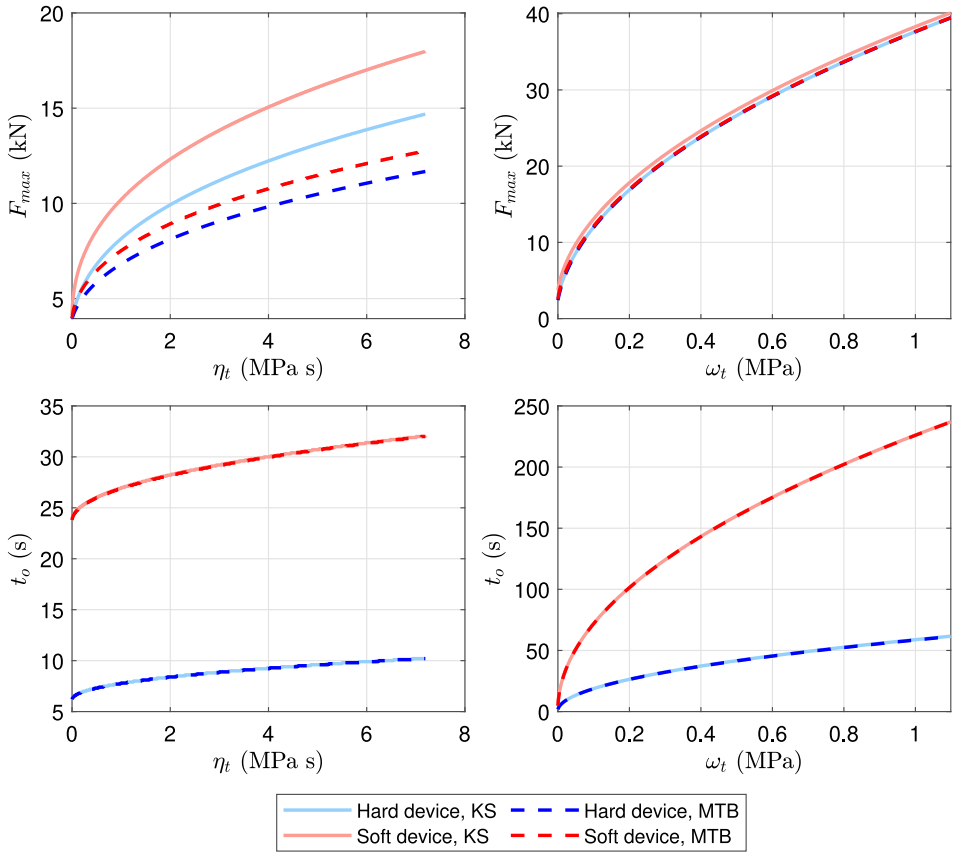

Fig. 10. Maximum force, F_{max}, and damage onset time, t_o, for the F2d model under pure traction vs. the damage rate coefficient η_t and the damage threshold ω_t for the micromechanical schemes (KS and MTB). The two cases of soft and hard device are considered.

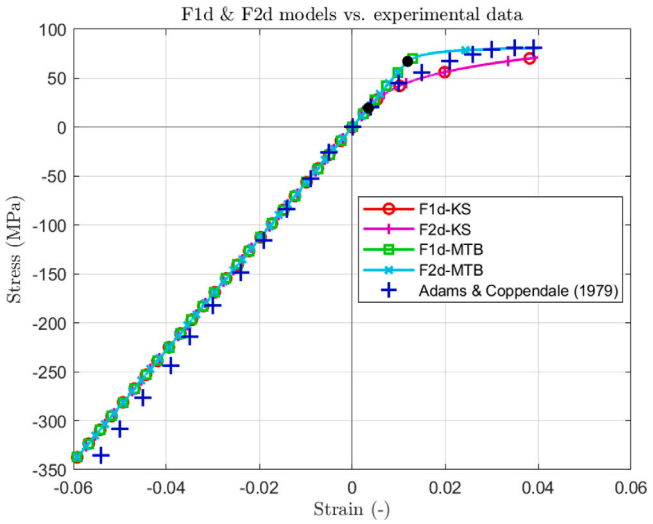

Fig. 11. Comparison of F1d and F2d model predictions with experimental data. The simulated stress–strain curves for the KS and MTB model variants are plotted against digitized experimental data for a BSL308 A adhesive butt joint from Adams and Coppendale (1979). Black markers indicate the predicted point of damage initiation for the KS and MTB models, respectively.

linear behavior up to a stress of approximately 20 MPa (indicated by a black marker), which matches the onset of nonlinearity observed in the experiment. This is followed by progressive softening which closely tracks the shape of the experimental curve until failure occurs. In contrast, models using the MTB scheme predict a more extended linear elastic range, with damage initiation occurring at a much higher stress of around 67 MPa. This is followed by an horizontal plateau that indicates a ductile adhesive's failure. While both micromechanical schemes provide a good overall fit, the KS variant captures the onset of damage more accurately in this particular experimental case.

5. Conclusion

In this paper, two interface damage models capable of representing tension–compression asymmetry, F1d and F2d, were developed starting from continuum damage mechanics and using asymptotic expansion techniques. Two distinct micromechanical schemes were implemented for each framework to link damage evolution to material stiffness degradation: the Kachanov-Sevostianov (KS) scheme and the Mori–Tanaka-Benveniste (MTB) scheme. The predictive capabilities of these model combinations were demonstrated through numerical simulations of the axial loading of a joint consisting of linear elastic adherents connected by the degrading interface.

The numerical results clearly showed that both the F1d and F2d frameworks effectively captured a significant tension–compression asymmetry. This was primarily due to the formulation of the damage evolution law, which deactivated the positive part of the displacement jump across the interface under compressive normal stress. The more advanced F2d model, which utilizes separate internal variables for tensile (ρ_t) and compressive (ρ_c) damage, exhibited an even more significant flexibility. By independently tuning the damage thresholds ($\hat{w}_t, \hat{w}_c$) and damage rate coefficients ($\hat{n}_t, \hat{n}_c$) parameters for each mode, the F2d model can represent a wide variety of material behaviors, from ductile tensile responses to brittle tensile failure, and reproduce different levels of tension–compression asymmetry.

Furthermore, the choice of micromechanical scheme was shown to be critical for predicting the ultimate failure characteristics. The Kachanov-Sevostianov (KS) formulation, due to its $1/(1 + C\rho)$ structure, inherently retains a non-zero residual stiffness even as damage ρ approaches unity. This characteristic results in an ascending branch or a ductile plateau in the force–displacement response under displacement control, without a complete loss of load-carrying capacity within the model's formulation. In contrast, the Mori–Tanaka-Benveniste (MTB) scheme, which incorporates the $\rho/(1-\rho)$ term, drives the effective moduli to zero as ρ approaches one. This complete degradation of stiffness leads to qualitatively different failure modes depending on the loading control. Under displacement control, a post-peak softening branch occurs where the force decreases with increasing displacement. Under force control, this zero-stiffness state would correspond to a ductile response.

The numerical simulations have effectively proved the theoretical potential of the proposed F1d and F2d models, showing that a wide range of realistic physical behaviors can be represented, including ductility and strong tension–compression asymmetry. Another contribution of this study is the qualitative assessment of the models against literature experimental data. As shown in Fig. 11, the predictions from both the KS and MTB variants of the F1d and F2d models are in strong qualitative agreement with the experimental stress–strain curves for adhesive butt joints reported by Adams and Coppendale (1979). In particular, the KS-based models accurately capture the experimentally observed onset of nonlinearity, while the MTB-based models effectively represent

the post-peak softening and ductile failure. This agreement serves to validate the fundamental ability of the F1d and F2d models to represent real material responses. While the parameters used for this comparison were chosen to provide a good qualitative fit and are not the result of a rigorous calibration, this validation establishes the basis for future work. The next step will be an experimental validation campaign, involving specific mechanical tests to calibrate the full set of F1d and F2d model parameters and to quantitatively assess their predictive accuracy. Furthermore, the F1d and F2d frameworks could be extended to incorporate other physical phenomena, such as load-induced anisotropy or rate-dependent viscoelastic effects.

In this respect, it is important to notice that the versions of the KS and MTB schemes used in this work are formulated for an isotropic distribution of micro-defects. Consequently, they describe a degradation of the effective stiffness that remains isotropic, governed by the evolution of the scalar damage variable(s), ρ (or ρ_t, ρ_c). The multi-axial nature of the stress state in an adhesive joint is expected to induce a preferential orientation of microcracks, even under a globally uniaxial applied load, leading to an evolution of load-induced anisotropy in the material's effective stiffness. However, the present study aims to introduce the F1d and F2d modeling approaches and specifically investigate their capacity to capture tension–compression asymmetry in the axial direction. Therefore, the simplification of isotropic damage is adopted. Extending the F1d and F2d models to account for anisotropic damage will be the focus of future work.

The successful implementation and comparison with literature experimental data in this work provide a basis for these future investigations and suggest that the proposed models hold significant potential for the advanced structural analysis of bonded joints.

CRediT authorship contribution statement

Michele Serpilli: Writing – review & editing, Writing – original draft, Visualization, Validation, Supervision, Project administration, Methodology, Investigation, Formal analysis, Conceptualization. **Raffaella Rizzoni:** Writing – review & editing, Writing – original draft, Visualization, Validation, Supervision, Software, Project administration, Methodology, Investigation, Formal analysis, Data curation, Conceptualization. **Frédéric Lebon:** Writing – review & editing, Validation, Supervision, Project administration, Methodology, Investigation, Formal analysis, Conceptualization.

Declaration of competing interest

The authors declare that they have no known competing financial interests or personal relationships that could have appeared to influence the work reported in this paper.

Acknowledgments

This research has been conducted according to the inspiring scientific principles of the Italian National Group for the Mathematical Physics (GNFM) of the National Institute for Advanced Mathematics (INdAM).

Appendix

In this section, the positive and negative parts of the first approximation of the strain tensor are computed. Let us recall that the positive and negative part of tensor $\mathbf{A}$ are defined as follows:

$$\begin{aligned} &\text{Positive part:} \quad \mathbf{A}^+ := \textstyle\sum_i \max(\lambda_i, 0)\mathbf{n}_i \otimes \mathbf{n}_i, \\ &\text{Negative part:} \quad \mathbf{A}^- := \textstyle\sum_i \max(-\lambda_i, 0)\mathbf{n}_i \otimes \mathbf{n}_i, \end{aligned} \tag{59}$$

where λ_i and $\mathbf{n}_i$ are the eigenvalues and eigenvectors of $\mathbf{A}$, with $|\mathbf{n}_i| = 1$, respectively. The positive and negative parts verify: $\mathbf{A} = \mathbf{A}^+ - \mathbf{A}^-$ and $\mathbf{A}^+ \cdot \mathbf{A}^- = 0$.

The approximation of the strain tensor at order $1/\varepsilon$ takes the following particular form:

$$\mathbf{E} = \begin{pmatrix} 0 & 0 & \frac{1}{2}w_{1,3} \\ 0 & 0 & \frac{1}{2}w_{2,3} \\ \frac{1}{2}w_{1,3} & \frac{1}{2}w_{2,3} & w_{3,3} \end{pmatrix}. \tag{60}$$

By means of a spectral decomposition, the eigenvalues and the corresponding eigenvectors of tensor $\mathbf{E}$ can be explicitly computed. The eigenvalues take the following values, as customary:

$$\gamma_0 = 0, \text{ and } \gamma_\pm := \frac{1}{2}\left(w_{3,3} \pm |\mathbf{w}_{,3}|\right), \tag{61}$$

with $|\mathbf{w}_{,3}| := \sqrt{w_{1,3}^2 + w_{2,3}^2 + w_{3,3}^2}$. Note that $\gamma_+ \geq 0$ and $\gamma_- \leq 0$. Finally, applying the above definition, the positive and negative parts of tensor $\mathbf{E}$ have the following expressions:

$$\mathbf{E}^+ = \frac{1}{4|\mathbf{w}_{,3}|}\begin{pmatrix} w_{1,3}^2 & w_{1,3}w_{2,3} & 2w_{1,3}\gamma_+ \\ w_{1,3}w_{2,3} & w_{2,3}^2 & 2w_{2,3}\gamma_+ \\ 2w_{1,3}\gamma_+ & 2w_{2,3}\gamma_+ & 4\gamma_+^2 \end{pmatrix}, \tag{62}$$

$$\mathbf{E}^{-} = \frac{1}{4|\mathbf{w}_{,3}|}\begin{pmatrix} w_{1,3}^2 & w_{1,3}w_{2,3} & -2w_{1,3}\gamma_- \\ w_{1,3}w_{2,3} & w_{2,3}^2 & -2w_{2,3}\gamma_- \\ -2w_{1,3}\gamma_- & -2w_{2,3}\gamma_- & 4\gamma_-^2 \end{pmatrix}. \tag{63}$$

Data availability

No data was used for the research described in the article.

References

Abrate, S., Ferrero, J. F., & Navarro, P. (2015). Cohesive zone models and impact damage predictions for composite structures. *Meccanica*, *50*, 2587–2620. http://dx.doi.org/10.1007/s11012-015-0221-1.

Adams, R. D., & Coppendale, J. (1976). Measurement of the elastic moduli of structural adhesives by a resonant bar technique. *Journal of Mechanical Engineering Science*, *18*(3), 149–158. http://dx.doi.org/10.1243/JMES_JOUR_1976_018_025_02.

Adams, R. D., & Coppendale, J. (1979). The stress-strain behaviour of axially-loaded butt joints. *Journal of Adhesion*, *10*(1), 49–62. http://dx.doi.org/10.1080/00218467908544611.

Alfano, G., & Crisfield, M. (2001). Finite element interface models for the delamination analysis of laminated composites: mechanical and computational issues. *International Journal for Numerical Methods in Engineering*, *50*(7), 1701–1736. http://dx.doi.org/10.1002/nme.93.

Alfano, G., & Sacco, E. (2006). Combining interface damage and friction in a cohesive-zone model. *International Journal for Numerical Methods in Engineering*, *68*(5), 542–582. http://dx.doi.org/10.1002/nme.1728.

Amor, H., Marigo, J. J., & Maurini, C. (2009). Regularized formulation of the variational brittle fracture with unilateral contact: numerical experiments. *Journal of the Mechanics and Physics of Solids*, *57*(8), 1209–1229. http://dx.doi.org/10.1016/j.jmps.2009.04.011.

Barenblatt, G. I. (1962). The mathematical theory of equilibrium cracks in brittle fracture. In H. L. Dryden, Th. von Kármán, G. Kuerti, F. H. van den Dungen, & L. Howarth (Eds.), *vol. 7*, *Adv. appl. mech.* (pp. 55–129). Elsevier, http://dx.doi.org/10.1016/S0065-2156(08)70121-2.

Bauzet, C., Dumont, S., Lebon, F., & Nabet, F. (2025). Toward stochastic imperfect interfaces. *ZAMM Zeitschrift fur Angewandte Mathematik*, *105*(4), Article e70030. http://dx.doi.org/10.1002/zamm.70030.

Benveniste, Y. (1986). On the Mori–Tanaka method for cracked solids. *Mechanics Research Communications*, *13*(4), 193–201. http://dx.doi.org/10.1016/0093-6413(86)90018-2.

Benveniste, Y. (1987). Effective thermal conductivity of composites with a thermal contact resistance between the constituents: Nondilute case. *Journal of Applied Physics*, *61*(8), 2840–2843. http://dx.doi.org/10.1063/1.337877.

Benveniste, Y., & Miloh, T. (1986). The effective conductivity of composites with imperfect thermal contact at constituent interfaces. *International Journal of Engineering Science*, *24*(9), 1537–1552. http://dx.doi.org/10.1016/0020-7225(86)90162-X.

Bonetti, E., Bonfanti, G., Lebon, F., & Rizzoni, R. (2017). A model of imperfect interface with damage. *Meccanica*, *52*, 1911–1922. http://dx.doi.org/10.1007/s11012-016-0520-1.

Cazes, F., Simatos, A., Coret, M., & Combescure, A. (2010). A cohesive zone model which is energetically equivalent to a gradient-enhanced coupled damage-plasticity model. *European Journal of Mechanics. A. Solids*, *29*(6), 976–989. http://dx.doi.org/10.1016/j.euromechsol.2009.11.003.

Ciarlet, P. G. (1997). *Series studies in mathematics and its applications, vol. II, Mathematical elasticity. Theory of plates*. North-Holland.

Corigliano, A. (1993). Formulation, identification and use of interface models in the numerical analysis of composite delamination. *International Journal of Solids and Structures*, *30*(20), 2779–2811. http://dx.doi.org/10.1016/0020-7683(93)90154-Y.

Corigliano, A., & Ricci, M. (2001). Rate-dependent interface models: formulation and numerical applications. *International Journal of Solids and Structures*, *38*(4), 547–576. http://dx.doi.org/10.1016/S0020-7683(00)00088-3.

Dormieux, L., Kondo, D., & Ulm, F.-J. (2006). A micromechanical analysis of damage propagation in fluid-saturated cracked media. *Comptes Rendus de l'Academie des Sciences, Serie II (Mecanique, Physique, Chimie, Sciences de l'nivers, Sciences de la Terre)*, *334*, 440–446. http://dx.doi.org/10.1016/j.crme.2006.05.007.

Dumont, S., Serpilli, M., Rizzoni, R., & Lebon, F. C. (2020). Numerical validation of multiphysic imperfect interfaces models. *Front. Mater.*, *7*, 158. http://dx.doi.org/10.3389/fmats.2020.00158.

Elices, M. G. G. V., Guinea, G. V., Gomez, J., & Planas, J. The cohesive zone model: advantages, limitations and challenges. *Engineering Fracture Mechanics*, 69(2), 137–163. http://dx.doi.org/10.1016/S0013-7944(01)00083-2.

Fassin, M., Eggersmann, R., Wulfinghoff, S., & Reese, S. (2019). Efficient algorithmic incorporation of tension compression asymmetry into an anisotropic damage model. *Computer Methods in Applied Mechanics and Engineering*, *354*, 932–962. http://dx.doi.org/10.1016/j.cma.2019.03.051.

Freddi, F., & Frémond, M. (2006). Damage in domains and interfaces: a coupled predictive theory. *J. Mech. Mater. Struct.*, *1*(7), 1205–1233. http://dx.doi.org/10.2140/jomms.2006.1.1205.

Frémond, M. (2002). *Non-smooth thermomechanics*. Berlin Heidelberg: Springer-Verlag, http://dx.doi.org/10.1007/978-3-662-04800-9.

Frémond, M., & Nedjar, B. (1995). Damage in concrete: the unilateral phenomenon. *Nucl. Eng. Des.*, *156*, 323–335. http://dx.doi.org/10.1016/0029-5493(94)00970-A.

Frémond, M., & Nedjar, B. (1996). Damage, gradient of damage and principle of virtual power. *International Journal of Solids and Structures*, *33*(8), 1083–1103. http://dx.doi.org/10.1016/0020-7683(95)00074-7.

Geymonat, G., Hendili, S., Krasucki, F., Serpilli, & Vidrascu, M. (2014). *Lecture notes in computational science and engineering*: *vol. 98*, *Asymptotic expansions and domain decomposition* (pp. 749–757). http://dx.doi.org/10.1007/978-3-319-05789-7_72.

Javili, A., Kaessmair, S., & Steinmann, P. (2014). General imperfect interfaces. *Computer Methods in Applied Mechanics and Engineering*, *275*, 76–97. http://dx.doi.org/10.1016/j.cma.2014.02.022.

Kachanov, M. (1994). Elastic solids with many cracks and related problems. *Advances and Applications in Fluid Mechanics*, *30*, 259–445. http://dx.doi.org/10.1016/S0065-2156(08)70176-5.

Kachanov, M., & Sevostianov, I. (2018). *Micromechanics of materials, with applications*. Cham: Springer, http://dx.doi.org/10.1007/978-3-319-76204-3.

Kachanov, M., Tsukrov, I., & Shafiro, B. (1994). Effective moduli of solids with cavities of various shapes. *ASME Applied Mechanics Reviews*, *47*(1S), S151–S174. http://dx.doi.org/10.1115/1.3122810.

Kim, Y. R. (2011). Cohesive zone model to predict fracture in bituminous materials and asphaltic pavements: state-of-the-art review. *Int. J. Pavement Eng.*, *12*(4), 343–356. http://dx.doi.org/10.1080/10298436.2011.575138.

Krasucki, F., Münch, A., & Ousset, Y. (2004). Mathematical analysis of nonlinear bonded joint models. *Mathematical Models & Methods in Applied Sciences*, *14*(04), 535–556. http://dx.doi.org/10.1142/S0218202504003349.

Kumar, S., & Mittal, K. L. (Eds.), (2013). *Advances in modeling and design of adhesively bonded systems*. John Wiley & Sons.

Lancioni, G., & Royer-Carfagni, G. (2009). The variational approach to fracture mechanics. A practical application to the French Panthéon in Paris. *Journal of Elasticity*, *95*, 1–30. http://dx.doi.org/10.1007/s10659-009-9189-1.
Lebon, F., & Rizzoni, R. (2010). Asymptotic analysis of a thin interface: the case involving similar rigidity. *International Journal of Engineering Science*, *48*(5), 473–486. http://dx.doi.org/10.1016/j.ijengsci.2009.12.001.
Lebon, F., & Rizzoni, R. (2011). Asymptotic behavior of a hard thin linear elastic interphase: An energy approach. *International Journal of Solids and Structures*, *48*(3–4), 441–449. http://dx.doi.org/10.1016/j.ijsolstr.2010.10.006.
Lemaitre, J. (1985). A continuous damage mechanics model for ductile fracture. *Journal of Engineering Materials and Technology*, *107*(1), 83–89. http://dx.doi.org/10.1115/1.3225775.
Lemaitre, J., Chaboche, J. L., Benallal, A., & Desmorat, R. (2009). *Mécanique des matériaux solides* (3ème éd.). Dunod.
Liu, R., Wang, X. J., Chen, P. W., Kang, G., Zhu, S. P., & Guo, Y. S. (2021). The role of tension-compression asymmetrical microcrack evolution in the ignition of polymer-bonded explosives under low-velocity impact. *Journal of Applied Physics*, *129*(17), Article 175108. http://dx.doi.org/10.1063/5.0046011.
(2024). *MATLAB version: 24.1.0.2578822 (R2024a)*. Natick, Massachusetts: The MathWorks Inc..
Mazars, J., Berthaud, Y., & Ramtani, S. (1990). The unilateral behaviourof damaged concrete. *Engineering Fracture Mechanics*, *35*(4–5), 629–635. http://dx.doi.org/10.1016/0013-7944(90)90145-7.
Mazars, J., & Pijaudier-Cabot, G. (1989). Continuum damage theory—application to concrete. *Journal of Engineering Mechanics*, *115*(2), 345–365. http://dx.doi.org/10.1061/(ASCE)0733-9399(1989)115:2(345).
Miehe, C., Welschinger, F., & Hofacker, M. (2010). Thermodynamically consistent phase-field models of fracture: variational principles and multi-FIELD FE implementations. *International Journal for Numerical Methods in Engineering*, *83*(10), 1273–1311. http://dx.doi.org/10.1002/nme.2861.
Mori, T., & Tanaka, K. (1973). Average stress in matrix and average elastic energy of materials with misfitting inclusions. *Acta Metallurgica*, *21*, 571–574. http://dx.doi.org/10.1016/0001-6160(73)90064-3.
Murakami, S. (1988). Mechanical modeling of material damage. *Journal of Applied Mechanics*, *55*(2), 280–286. http://dx.doi.org/10.1115/1.3173673.
Needleman, A. (1990). An analysis of tensile decohesion along an interface. *Journal of the Mechanics and Physics of Solids*, *38*(3), 289–324. http://dx.doi.org/10.1016/0022-5096(90)90001-K.
Park, T., Ahmed, B., & Voyiadjis, G. Z. (2021). A review of continuum damage and plasticity in concrete: Part I – theoretical framework. *International Journal of Damage Mechanics*, *31*(6), 901–954. http://dx.doi.org/10.1177/10567895211068174.
Park, K., & Paulino, G. H. (2011). Cohesive zone models: a critical review of traction-separation relationships across fracture surfaces. *Applied Mechanics Reviews*, *64*(6), Article 060802. http://dx.doi.org/10.1115/1.4023110.
Pichler, B., Hellmich, C., & A. Mang, H. (2007). A combined fracture-micromechanics model for tensile strain-softening in brittle materials, based on propagation of interacting microcracks. *International Journal for Numerical and Analytical Methods in Geomechanics*, *31*, 111–132. http://dx.doi.org/10.1002/nag.544.
Ponte Castañeda, P., & Willis, J. R. (1995). The effect of spatial distribution on the effective behavior of composite materials and cracked media. *Journal of the Mechanics and Physics of Solids*, *43*(12), 1919–1951. http://dx.doi.org/10.1016/0022-5096(95)00058-Q.
Pronina, Y., Narykova, M., & Kachanov, M. (2025). Relating stiffness changes in porous materials to the evolution of pore space. *Mechanics of Materials*, *202*, Article 105236. http://dx.doi.org/10.1016/j.mechmat.2024.105236.
Raffa, M. L., Lebon, F., & Rizzoni, R. (2022). A micromechanical model of a hard interface with micro-cracking damage. *International Journal of Mechanical Sciences*, *216*, Article 106974. http://dx.doi.org/10.1016/j.ijmecsci.2021.106974.
Raffa, M. L., Lebon, F., & Vairo, G. (2016). Normal and tangential stiffnesses of rough surfaces in contact via an imperfect interface model. *International Journal of Solids and Structures*, *87*, 245–253. http://dx.doi.org/10.1016/j.ijsolstr.2016.01.025.
Ries, M. (2024). Mechanical behavior of adhesive joints: A review on modeling techniques. *Computational Methods in Mathematics and Science*, *24*(4), 5–35. http://dx.doi.org/10.7494/cmms.2024.4.1010.
Rizzoni, R., Dumont, S., & Lebon, F. (2017). On Saint Venant–Kirchhoff imperfect interfaces. *International Journal of Non-Linear Mechanics*, *89*, 101–115. http://dx.doi.org/10.1016/j.ijnonlinmec.2016.12.002.
Rizzoni, R., Dumont, S., Lebon, F., & Sacco, E. (2014). Higher order model for soft and hard elastic interfaces. *International Journal of Solids and Structures*, *51*(23–24), 4137–4148. http://dx.doi.org/10.1016/j.ijsolstr.2014.08.005.
Rizzoni, R., Serpilli, M., Raffa, M. L., & Lebon, F. (2023). A micromechanical model for damage evolution in thin piezoelectric films. *Coatings*, *13*(1), 82. http://dx.doi.org/10.3390/coatings13010082.
Rohatgi, A. (2024). WebPlotDigitizer, version 4.8. https://automeris.io/WebPlotDigitizer. (Accessed 29 August 2025).
Sánchez-Palencia, E. (1980). *Lecture note in physics: vol. 320, Non-homogeneous media and vibration theory* (pp. 57–65). Springer-Verlag.
Serpilli, M. (2014). Asymptotic analysis of a multimaterial with a thin piezoelectric interphase. *Meccanica*, *49*, 1641–1652. http://dx.doi.org/10.1007/s11012-014-9936-7.
Serpilli, M., & Lenci, S. (2016). An overview of different asymptotic models for anisotropic three-layer plates with soft adhesive. *International Journal of Solids and Structures*, *81*, 130–140. http://dx.doi.org/10.1016/j.ijsolstr.2015.11.020.
Serpilli, M., Rizzoni, R., Lebon, F., & Dumont, S. (2019). An asymptotic derivation of a general imperfect interface law for linear multiphysics composites. *International Journal of Solids and Structures*, *180*, 97–107. http://dx.doi.org/10.1016/j.ijsolstr.2019.07.014.
Shah, S. P., Swartz, S. E., & Ouyang, C. (1995). *Fracture mechanics of concrete: applications of fracture mechanics to concrete, rock and other quasi-brittle materials*. John Wiley & Sons.
Stefaniuk, D., & Kachanov, M. (2024). On the effective properties of random microstructures and cross-property connections for them. *International Journal of Engineering Science*, *199*, Article 104061. http://dx.doi.org/10.1016/j.ijengsci.2024.104061.
Technical data sheet 3M™ Scotch-Weld™: https://multimedia.3~m.com/mws/media/2366022O/3M-Scotch-Weld-Epoxy-Adhesive-2216-B-A-Gray.pdf?pif=000157.
Tserpes, K., Barroso-Caro, A., Carraro, P. A., Beber, V. C., Floros, I., Gamon, W., et al. (2022). A review on failure theories and simulation models for adhesive joints. *Journal of Adhesion*, *98*(12), 1855–1915. http://dx.doi.org/10.1080/00218464.2021.1941903.
Van Mier, J. G. (1996). *Fracture processes of concrete, vol. 12*. CRC Press, http://dx.doi.org/10.1201/b22384.
Vicentini, F., Zolesi, C., Carrara, P., Maurini, C., & De Lorenzis, L. (2024). On the energy decomposition in variational phase-field models for brittle fracture under multi-axial stress states. *International Journal of Fracture*, *247*, 291–317. http://dx.doi.org/10.1007/s10704-024-00763-w.
Wei, Z., Gerke, S., & Brünig, M. (2023). Damage and fracture behavior under non-proportional biaxial reverse loading in ductile metals: experiments and material modeling. *International Journal of Plasticity*, *171*, Article 103774. http://dx.doi.org/10.1016/j.ijplas.2023.103774.
Wei, Z., Zistl, M., Gerke, S., & Brünig, M. (2022). Analysis of ductile damage and fracture under reverse loading. *International Journal of Mechanical Sciences*, *228*, Article 107476. http://dx.doi.org/10.1016/j.ijmecsci.2022.107476.
Xu, Q., & Lu, Z. (2013). An elastic–plastic cohesive zone model for metal–ceramic interfaces at finite deformations. *International Journal of Plasticity*, *41*, 147–164. http://dx.doi.org/10.1016/j.ijplas.2012.09.008.
Yang, L., Yan, Y., Liu, Y., & Ran, Z. (2012). Microscopic failure mechanisms of fiber-reinforced polymer composites under transverse tension and compression. *Composites Science and Technology*, *72*(15), 1818–1825. http://dx.doi.org/10.1016/j.compscitech.2012.08.001.
Zhang, J., Han, J., Zhang, Q., Reese, S., & Brepols, T. (2025). Tension-compression asymmetry based on different energy decompositions within a gradient-extended two-surface damage-plasticity framework comput. *Mechanics*, http://dx.doi.org/10.1007/s00466-025-02652-y.
Zhang, H., Ramesh, K. T., & Chin, E. S. C. (2008). A multi-axial constitutive model for metal matrix composites. *Journal of the Mechanics and Physics of Solids*, *56*(10), 2972–2983. http://dx.doi.org/10.1016/j.jmps.2008.07.001.